Optical and Quantum Electronics (2024) 56:1463
https://doi.org/10.1007/s11082-024-07388-2

First-principles investigation of pressure-modulated structural, electronic, mechanical, and optical characteristics of Sr_3PX_3 (X = Cl, Br) for enhanced optoelectronic application

Sheikh Joifullah[1] · **Md. Adil Hossain**[1] · **Maruf Al Yeamin**[1] · **Md. Mahfuzul Haque**[1] · **Redi Kristian Pingak**[2] · **Noorhan F. AlShaikh Mohammad**[3] · **Mohammed S. Abu-Jafar**[4] · **Ahmad A. Mousa**[5,6] · **Asif Hosen**[1]

Received: 29 June 2024 / Accepted: 20 August 2024

Abstract

This study investigates the influence of hydrostatic pressure on structural, electronic, mechanical and optical properties of Sr_3PX_3 (X = Cl and Br) compounds, by using the first-principles density functional theory (DFT) within the pressure range of 0–30 GPa with a span of 10 GPa. For Sr_3PCl_3 and Sr_3PBr_3, the dynamical stability is confirmed by the fact that the phonon dispersion curves do not contain imaginary modes. Pressure-induced band gap alterations in Sr_3PCl_3 and Sr_3PBr_3 reveal semiconducting behavior: GGA measurements show a decrease from 1.70 eV and 1.55 eV at ambient pressure to 0.22 eV and 0.21 eV at 30 GPa; TB-mBJ results show a decrease from 2.73 eV and 2.40 to 1.07 eV and 0.92 eV. This supports their inverse relationship with pressure. The values of Debye and melting temperatures support their high-temperature applications. Effective mass also shows an inverse relationship with induced pressure. The bond length, lattice parameters, and cell volume reduces with pressure. They exhibit ductility, which is further enhanced by the applied pressure. These materials emerge as promising candidates for flexible optoelectronic devices. Optical properties like absorption coefficients, reflectivity, and dielectric functions were observed and found to be significantly influenced by applied pressure. The absorption spectra exhibit a significant redshift with increasing pressure, indicating enhanced potential for optoelectronic applications. Our detailed investigation sheds light on the tunability of Sr_3PX_3 (X = Cl and Br) properties under pressure, showcasing their potential for cutting-edge applications in optoelectronics and photovoltaics.

Keywords DFT · Dynamic stability · Debye temperature · Effective mass · Optical properties

1 Introduction

The fastest-growing photovoltaic materials are hybrid organic–inorganic halides at the moment, which are used for solar cells (Huang et al. 2020; Liu et al. 2020; Seo et al. 2016). For their simple crystal structure and a variety of characteristics, including resistivity,

---

Extended author information available on the last page of the article piezoelectricity, ferroelectricity, and superconductivity, perovskite oxides are highly valued in the field of material research (Butt et al. 2021; Kouchaksaraie 2011; Verma and Jindal 2009). Perovskites are exceptional because of their broad variety of uses in the most recent developments and their special capacity to undergo phase changes (Khan et al. 2023; Wu et al. 2021). Particularly, lead halide perovskites gained a lot recognition in photovoltaics (PV) field because of their affordable price, appropriate band gaps, high photoinduced carrier mobility (Wehrenfennig et al. 2014; Zhumekenov et al. 2016), and effective visible light absorption (Kojima et al. 2009; Lee et al. 2012; Stoumpos et al. 2013). Lead halide perovskites show great properties but contain toxicity (Liu et al. 2019b; Yang et al. 2020). In addition, regarding lead toxicity, perovskite solar cell manufacture and disposal create significant problems, which limits the sustainability of the technology and puts human and environmental health at risk (Ren et al. 2022). Because of this, researchers have consequently paid close attention to lead-free halide perovskites (Lan et al. 2021; Moghe et al. 2016).

These Lead-free materials are getting a lot of attention because of their remarkable optoelectronic qualities, Conductivity, mechanical stability, absorption coefficient, and tunable band gap properties (Yin et al. 2014; Zhang et al. 2016). In contrast to lead (Pb)-containing PV cells, the bulk of perovskites have more encouraging qualities and are typically more ecologically harmless (Babayigit et al. 2016; Eperon et al. 2015). A broad range of characteristics, including conductivity, insulation, semi-conduction, and superconductivity, are present in perovskite materials (Bhalla et al. 2000; Kanhere and Chen 2014). As a result, perovskites are acknowledged by many as a highly significant class of materials that comprise various crystal shapes (Filip and Giustino 2018). Even though the method of turning electricity into light is the opposite of that of turning light into electricity, the first research on converting electricity into light was published several decades before the initial study on halide perovskites being utilized as photovoltaic sun absorbers (Jiang et al. 2019). Right now, solar technologies are replacing conventional energy sources. Over the past ten years, perovskite materials have seen improvements that have accelerated development (Jung and Park 2015). It's also making advances in the green solar consumers (Ali et al. 2023; Dandia et al. 2020; Liu et al. 2019a; Tian et al. 2019). The ABX_3 group of perovskite materials has garnered huge attention, wherein Sn^{2+}, Ge^{2+}, Eu^{2+}, Dy^{2+}, and Yb^{2+} have been explored as substitutes for the hazardous Pb^{2+}, resulting in exceptional optoelectronic properties to hold significant value for the perovskite solar cell field (Marshall et al. 2016; Noel et al. 2014; Zhou et al. 2018). The variation of elemental constituents (A, B, or X) within the ABX_3 configuration can also be noticed as provoking a form of internal pressure due to the alteration in elemental size, and thus, an overall grasp of the impact of structural deviation demands this influence to be compared precisely.

Recent years have seen a variety of research projects that have used strain engineering to enhance particular material qualities. (Feng and Zhang 2021) identified the stable compounds of high efficiency on A_3MX_3 structure (the following: A = Ca, Mg, Ba, Sr; M = N, P, As, Sb and X = F, Cl, Br, I) and found Ba_3PI_3, Ba_3AsI_3, and Ba_3SbI_3 stable PV material which showed up to 25.9% efficiency. (Zhou et al. 2016) worked on $MAPbI_3$ by applying pressure, gaining a higher band gap energy, more carrier mobility, and better absorption coefficients for the material that can raise its potential for use in photovoltaics. (Islam et al. 2024) worked with Ca_3PCl_3 perovskite by applying biaxial strain. Where in the absorption spectra, tensile strain leads to a blue shift (toward greater energy) while compressive strain leads to a redshift (toward lower energy). (Faridi et al. 2018) showed the reverse relationship of pressure with anisotropy and the brittle to ductile shift under hydrostatic pressure of $KNbO_3$. A strontium-based research by (Algahtani et al. 2024) on Sr_3AsX_3

(X = F and Br) showed high optical absorption within the range of 2–10 eV. The band gap obtained by HSE was quite high around 2.5 eV. Working with A_3BX_3 (A = Ca, Sr, B = P, As, X = I, Br), which consists of 6 compounds in total, (Ghosh et al. 2024b) discovered that the HSE approach shows a larger band gap than the GGA method. Later, (Ghosh et al. 2023) reduced the band gap of Sr_3AsI_3 by applying strain. In addition, (Ghosh et al. 2024a) worked with Sr_3PBr_3 on strain-induced changes and studied structural, electronic, mechanical, and optical properties with FP-DFT, where it exhibits remarkable light absorption within the visible light range.

This study comprehensively investigates the structural, electronic, mechanical, and optical characteristics of Sr_3PX_3 (X = Cl, Br) under various pressures utilizing density functional theory (DFT). According to earlier studies, no research was done on the pressure-induced characteristics of Sr_3PBr_3. Therefore, a thorough examination of the physical properties of Sr_3PCl_3 and Sr_3PBr_3 is important with pressure-induced changes to be able to obtain a comprehensive understanding of the behaviors in such systems, particularly with regard to their prospective application sectors. The most trustworthy theoretical framework for examining the chemical and physical properties of materials is density functional theory (DFT)-based first-principles technique. (Hossain et al. 2021b; Hossain et al. 2021a; Hossain et al. 2020; Rasheduzzaman et al. 2021). Energy gap modification and structural features are conducted in order to clarify its electronic properties. Optical properties which also changed due to increasing pressure. The red shifting properties of Sr_3PX_3 (X = Cl, Br) absorption spectra are investigated in relation to the changes in peak positions of the dielectric maxima under various pressure levels. From our investigation, this compound's optoelectronic characteristics are changed in pressure conditions, for that these materials are suitable for use in optoelectronic devices applications.

2 Computational details

The Sr_3PX_3 (X = Cl, Br) compound was examined by ab initio computations, which were carried out utilizing the Quantum ESPRESSO (QE) package's Density Functional Theory (DFT) method (Giannozzi et al. 2009). Self-consistent computations were conducted to solve the Kohn–Sham equations (Kohn and Sham 1965) utilizing the Perdew-Burke-Ernzerhof (GGA-PBE) exchange-correlational functional in the Generalized Gradient Approximation (Perdew et al. 1996) along the ultra-soft pseudo-potentials (Perdew et al. 1992; Vanderbilt 1990). A plane-wave basis was set with a 40 (Ry) kinetic energy cut-off, 440 (Ry) charge density cut-off, and 1.0×10^{-8} convergence threshold was used to attain convergence. The lattice parameters used for the Sr_3PCl_3 and Sr_3PBr_3 structures were 6.05 Å and 6.23 Å, respectively. To enhance the crystal structure and in order to get the lowest energy state feasible, we applied the Broyden–Fletcher–Goldfarb–Shanno (BFGS) optimization method. (Fischer and Almlof 2002) alongside a force convergence threshold of 1×10^{-3}. In addition, the lattice optimization was performed using the vc-relax method with a k-point value of 8×8×8. GGA-PBE approximations were used to do electronic band structure computations. k-points dimension of 8×8×8 for self-consistent field (SCF) calculations and 12×12×12 for non-self-consistent field (NSCF) calculations are utilized. First-order time-dependent perturbation theory was applied to analyze the optical properties of the material formations and assess their dynamic stability (Karsch et al. 1997; Langhoff et al. 1972). For subsequent calculations, we applied the Tran-Blaha modified Becke-Johnson (TB-mBJ) approximation (Tran and Blaha 2009) in WIEN2K code (Blaha et al.

2020), which is specifically developed to enhance the accuracy of electronic band gap predictions, particularly for semiconductors and insulators. To achieve both charge and energy convergence, we utilized a linearized augmented plane-wave basis set with $l_{\max} = 10$ and $R_{\mathrm{MT}}K_{\max} = 7$ (where $K_{\max}$ represents the maximum K-value). After achieving dynamic stability, the intricate dielectric functions of Sr_3PX_3 (X = Cl, Br) were calculated to study their optical properties, which are affected by the photon energy. The optical properties obtained by utilizing the complex dielectric function, were denoted as $\varepsilon(\omega) = \varepsilon_1(\omega) + i\varepsilon_2(\omega)$, which consists of $\varepsilon_1(\omega)$ (real part) and $\varepsilon_2(\omega)$ (imaginary part). The THERMO-PW approach was used to calculate the mechanical characteristics by assessing the elastic constant. The ELATE tool (Gaillac et al. 2016) is used to plot 3D illustration of anisotropy.

3 Results and discussion

3.1 Structural properties

The Sr_3PX_3 (X = Cl, Br) compounds belong to the cubic space group Pm3m (#221) (Johnsson and Lemmens 2005). Both compounds crystalize in a cubic structure, as demonstrated in Fig. 1a and b. The unit cells of each compound consist of 7 atoms. The Sr, P, and Cl/Br atoms are at in the following Wyckoff positions: Sr atom at (0.5, 0, 0), P atoms at (0 0, 0), and X (Cl/Br) atoms at (0, 0.5, 0.5) (Zhao et al. 2018a). Table 1 covers the Lattice constant (a_0), Unit cell optimum volume (V_0), Bulk modulus (B), Pressure derivative of bulk modulus ($B\prime$), Ground state energy (E_0), and Bandgap (E_g). The energy deviation was determined by using the Murnaghan equation (Murnaghan 1944):

$$E(V) = E_0(V) + \frac{BV}{B\prime}\left[\frac{\left(\frac{V_0}{V}\right)^{B\prime}}{B\prime - 1} + 1\right] - \frac{BV_0}{B\prime - 1}$$

The energy levels found in the above Murnaghan equation with respect to different volumes are illustrated in Fig. 2a and b. Both compounds are found to have negative ground state energy, but Sr_3PBr_3 has significantly lower ground state energy compared to Sr_3PCl_3

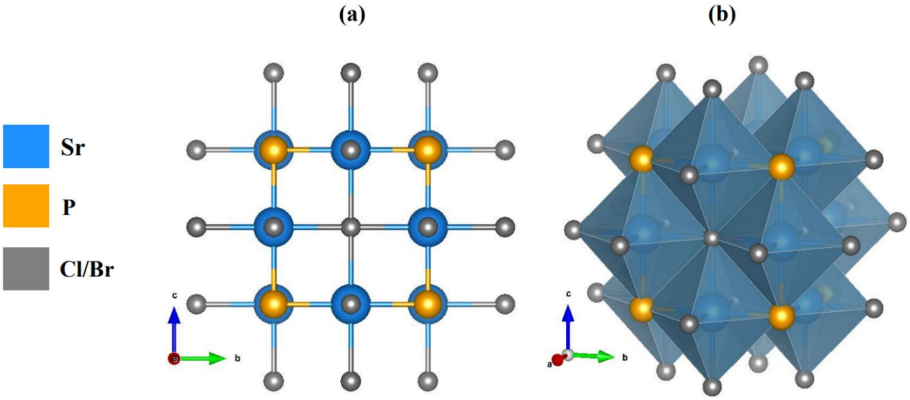

Fig. 1 2D and 3D crystal structure of cubic Sr_3PX_3 (X = Cl, Br) unit cell

Table 1 Sorted values of different optimized structural parameters and band gap for Sr_3PX_3 (X = Cl and Br)

Optimized structural parameters	Sr_3PCl_3	Sr_3PBr_3	
		Present work	Other work (Ghosh et al. 2024 a)
Lattice constant, a_0 in Å	6.05	6.21	6.61
Optimum volume, V_0 in $Å^3$	221.35	239.60	288.8
Bulk modulus, B in GPa	30.42	28.38	29.5
Pressure derivative of bulk modulus, B'	2.56	4.33	–
Ground state energy, E_0 in Ry	– 318.63	– 314.53	– 278.33
Band Gap, E_g in eV	1.70^{GGA} $2.73^{TB\text{-}mBJ}$	1.55^{GGA} $2.41^{TB\text{-}mBJ}$	1.528^{GGA} –

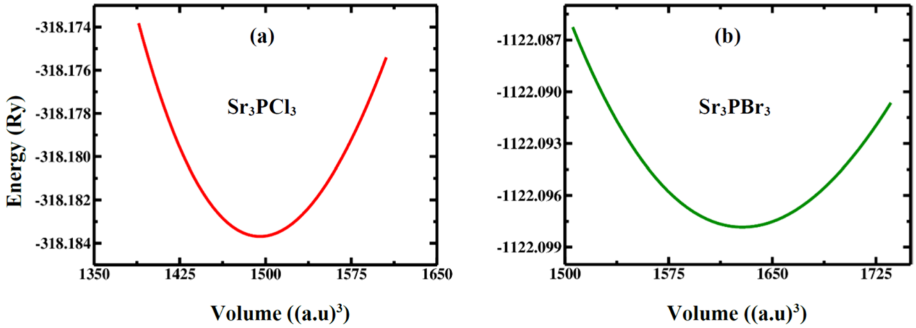

Fig. 2 Volume optimization curves for Sr_3PX_3 (X = Cl, Br)

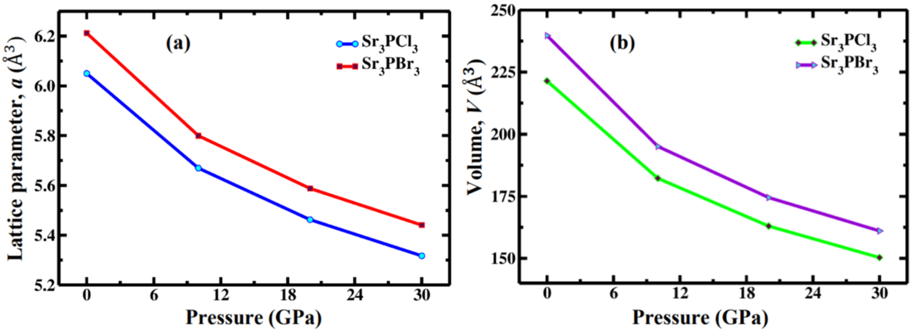

Fig. 3 Optimized lattice constant and volume for Sr_3PX_3 (X = Cl, Br) as a function of pressure

indicating a more stable structure. The graphical representation of this effect is shown in Fig. 3a and b. It also shows a lattice parameter of 6.05 Å for Sr_3PCl_3 and 6.21 Å for Sr_3Br_3, which aligns with the previous work by (Ghosh et al. 2024a) which was 6.61 Å. A slight difference is notable here, it could have been due to the use of HSE method in previous research.

Table 2 Calculated bond lengths between atoms in Sr_3PX_3 (X = Cl and Br) at various hydrostatic pressures

Pressure (GPa)	Bond length (Å)					
	Sr_3PCl_3			Sr_3PBr_3		
	Sr–Cl	Sr–P	P–Cl	Sr–Br	Sr–P	P–Br
0	3.025	3.025	4.278	3.106	3.106	4.392
10	2.834	2.834	4.009	2.899	2.899	4.101
20	2.731	2.731	3.862	2.793	2.793	3.951
30	2.658	2.658	3.759	2.720	2.720	3.847

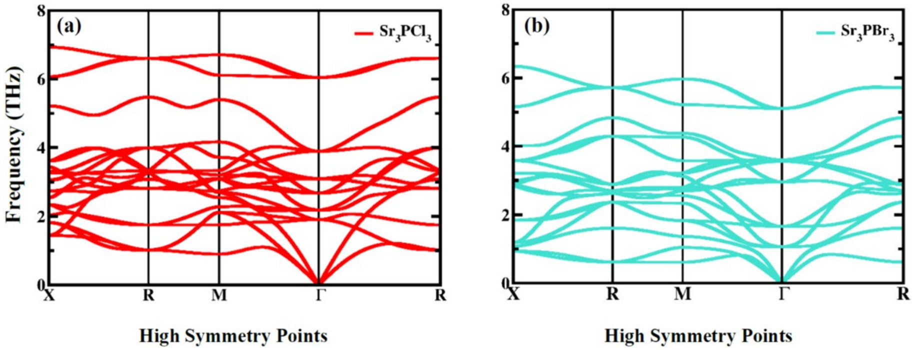

Fig. 4 Phonon dispersion spectrum of Sr_3PX_3 (X = Cl, Br)

As per Table 2, the volume of unit cells decreases with pressure which means the bond lengths also decrease. This leads to the narrowing of bandgap and overlapping conditions between atoms (Xiong et al. 2017). The band gap narrowing is expected to improve the optoelectronic properties of materials for better performance in optoelectronic devices. It was also noted that increased pressure resulted in a reduction in the volume of the unit cells for various materials including cubic $FrQCl_3$ (Hosen et al. 2024a), trigonal and monoclinic $MgSiO_3$ (Gao et al. 2020), cubic $RbCaBr_3$ (Hosen et al. 2024c), and high-entropy alloys (Ahmad et al. 2017).

3.2 Phonon stability

Phonon dispersion analysis allows us to understand the vibrational properties of a material, which in turn influence its thermal and electrical behavior. The dynamic stability of Sr_3PCl_3 and Sr_3PBr_3 is assessed by constructing a 2×2×2 supercell, enabling a detailed analysis of the materials' vibrational properties and structural stability. Using this larger supercell allows us to capture a broader range of vibrational modes and atomic interactions, leading to a more precise evaluation of the material's dynamic behavior. Figure 4 show the phonon dispersion curves for Sr_3PCl_3 and Sr_3PBr_3. Both material's phonon dispersion curves have no negative frequencies, confirming their dynamical stability (Jehan et al. 2023; Khattak et al. 2023). With no imaginary frequencies in the Brillouin zone, Sr_3PCl_3 and Sr_3PBr_3 remain stable despite minor perturbations, verifying their cubic structures. The dynamic stability of Sr_3PBr_3 has also been confirmed in prior research through the analysis of phonon dispersion frequencies (Ghosh et al. 2024a). Comparing Sr_3PCl_3 and Sr_3PBr_3 reveals similar phonon activity, with modest frequency shifts due to Cl and Br atom's mass differences, impacting material vibrations. Understanding the phonon behavior of Sr_3PCl_3 and Sr_3PBr_3 is crucial for understanding their vibrational spectra and thermal and electrical characteristics.

3.3 Electronic properties

Investigating the electronic characteristics of Sr_3PX_3 (X = Cl, Br) with applied pressure is the key to understanding its future use. Employing Density Functional Theory (DFT) computations via Quantum Espresso, we scrutinize its band configuration, bandgap, electron charge density, density of states (Partial and total), and effective mass. These examinations are important in understanding their electronic behavior and integrating them into the various technologies. One of the characteristics of semiconductor materials is that adjusting the band gap is possible to enable the manipulation of electron flow and is suitable for various uses.

In this research, bandgap (E_g) values for Sr_3PX_3 (X = Cl, Br) were obtained using both the GGA-PBE and TB-mBJ approximations, with TB-mBJ providing more accurate results**.** Sr_3PCl_3 exhibits a bandgap (E_g) of 1.7 eV under zero pressure, which greatly decreases to 0.22 eV under a pressure of 30 GPa, illustrated in Fig. 5. Similarly, Sr_3PBr_3 shows a reduction in bandgap (E_g) from 1.55 eV without pressure to 0.21 eV at 30 GPa, illustrated in Fig. 6. These values were obtained using GGA-PBE approximation. The initial value matches with the previous research on Sr_3PBr_3 by (Ghosh et al. 2024a) at

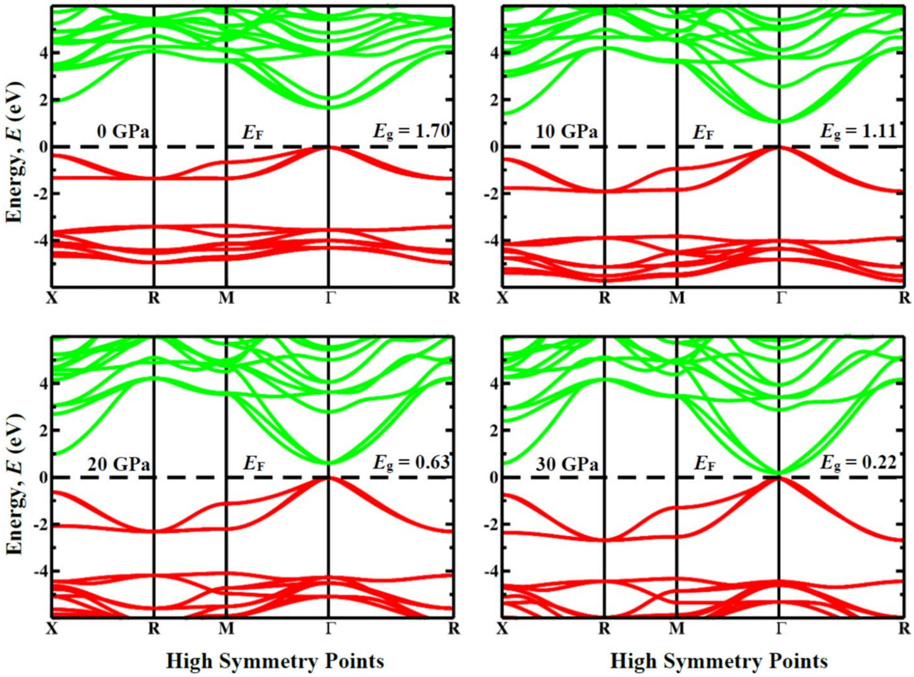

Fig. 5 Band structure of Sr_3PCl_3 at various applied pressures with GGA-PBA approximation

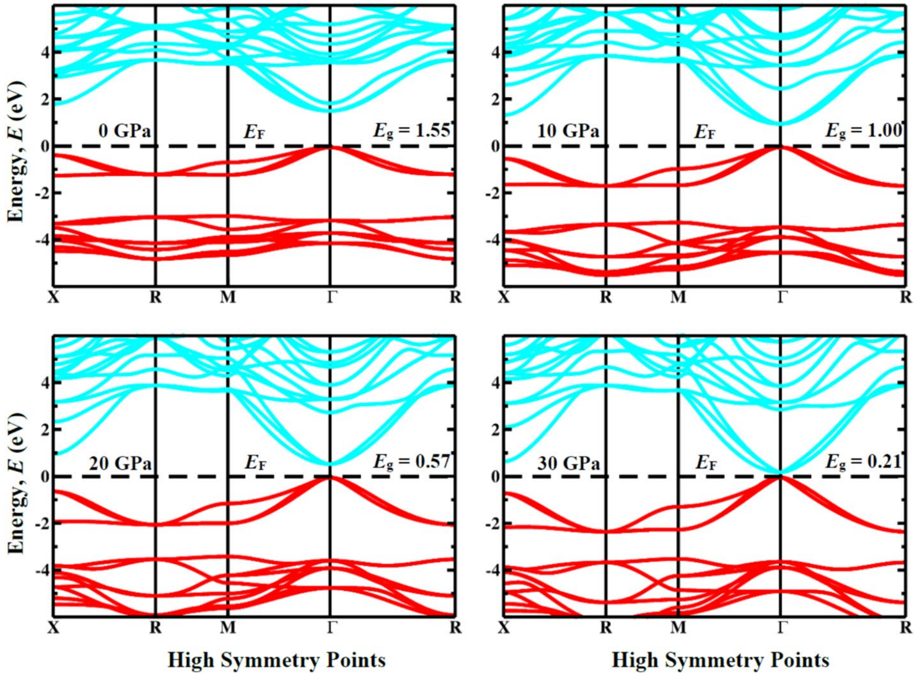

Fig. 6 Band structure of Sr_3PBr_3 at various applied pressures with GGA-PBA approximation

zero strain, which was 1.528 eV, which justified the accuracy of our work. Using TB-mBJ, Sr_3PCl_3 shows a bandgap of 2.73 eV at zero pressure, decreasing to 1.07 eV at 30 GPa, while Sr_3PBr_3 shows a reduction from 2.40 to 0.92 eV under the same conditions. The corresponding band structures are illustrated in Figs. 7 and 8. The relation of band gap for both compounds with applied pressure is illustrated in Fig. 9. This similar type of reduction of E_g with applied pressure is found in similar types of single-halides. The pressure-induced fluctuations in the bandgap (E_g) of Sr_3PCl_3 and Sr_3PBr_3 make them well-suited for pressure-sensing applications, where changes in the E_g can serve as a reliable indicator of pressure levels. Furthermore, the adjustable nature of the E_g renders these substances immensely appealing for optoelectronic gadgets, presenting prospects for crafting devices with customized optical and electronic characteristics. Our findings align with previous research, highlighting the consistent correlation between applied pressure and bandgap reduction in semiconductor materials.

Density of states (DOS) sheds light on the material's electronic and optical behavior by providing essential insights into the elemental contributions and bonding properties. Our research indicates that the halide elements (Br-4*p* and Cl-3*p*), Strontium (4*p*), and phosphorus (P-3*p*) play critical roles in influencing the electronic characteristics of the material because of their high density near the Fermi level illustrated in Figs. 10 and 11 respectively. The presence of partially filled valence bands in the DOS around the Fermi level indicates that halides with strontium and phosphorus orbitals are involved in charge transport activities. The valance band's primary source of contribution is P-3p orbital, minor contributions from Sr-5*s* and Sr-4*p* orbitals and in the conduction band major contribution comes from Sr-4*p* orbitals along with minor contributions from other orbitals. The involvement of Strontium (Sr-4*p* and Sr-5*s*) orbitals in both valance

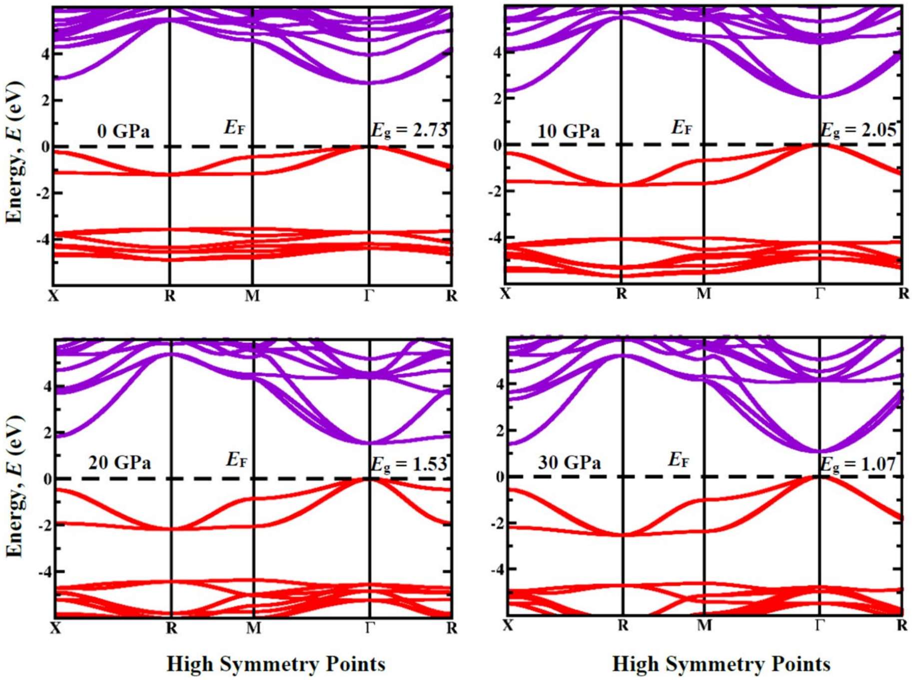

Fig. 7 Band structure of Sr_3PCl_3 at various applied pressures with TB-mBJ approximation

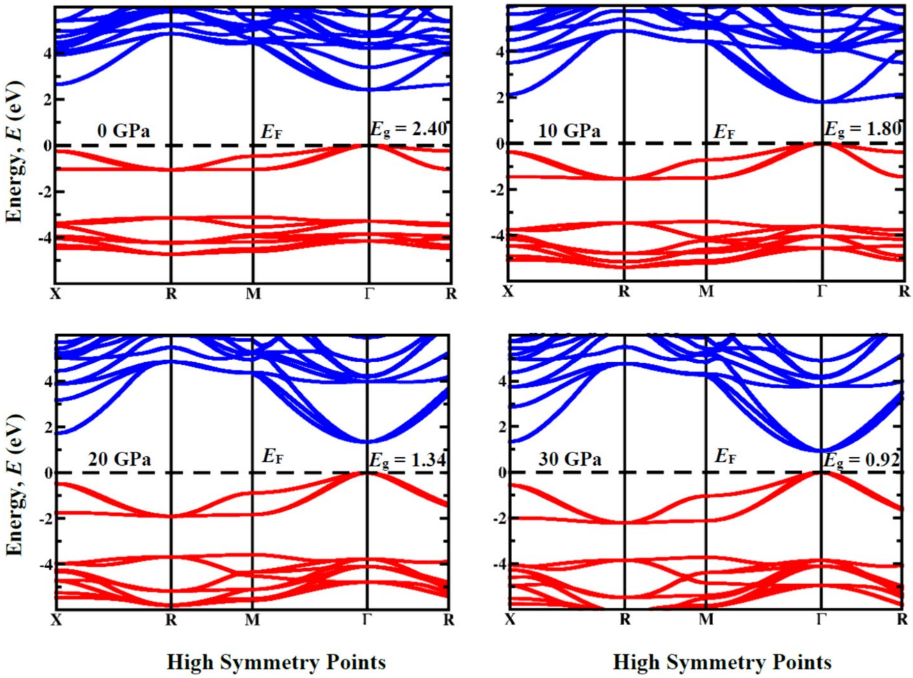

Fig. 8 Band structure of Sr_3PBr_3 at various applied pressures with TB-mBJ approximation

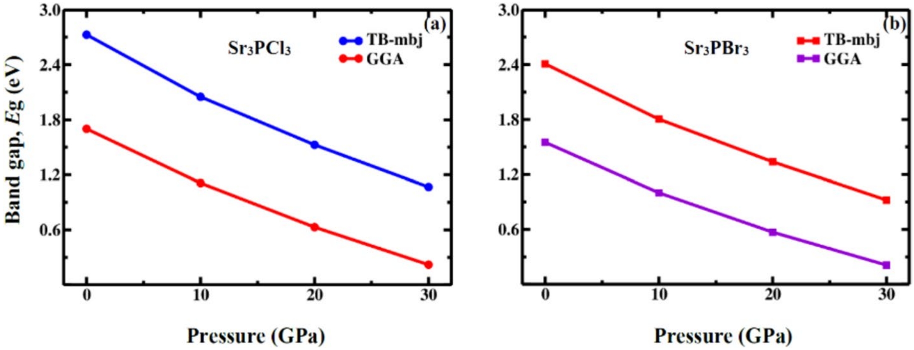

Fig. 9 Variation of band gap of Sr_3PX_3 (X = Cl, Br) at various applied pressures

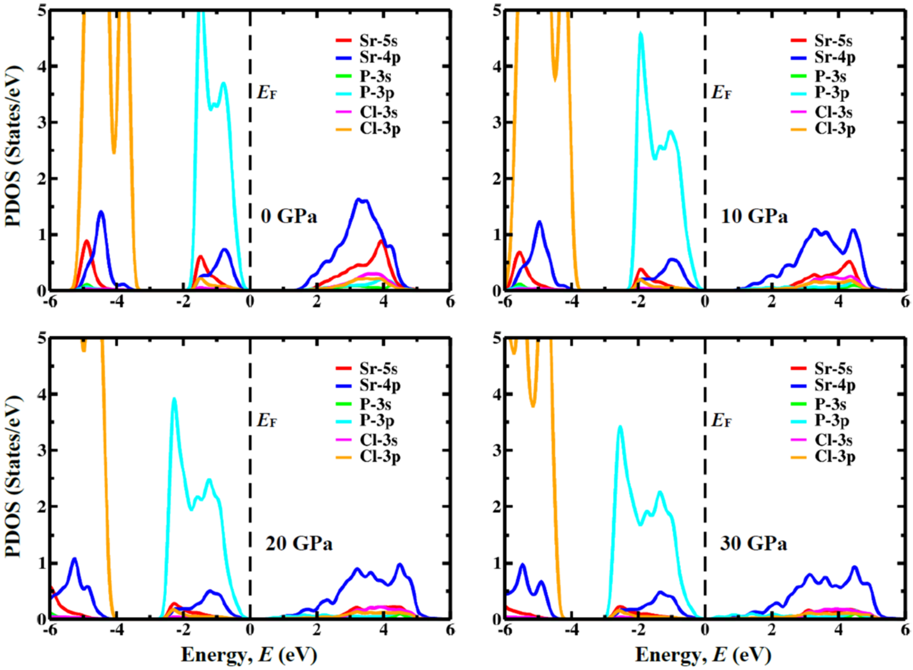

Fig. 10 The partial density of states of Sr_3PCl_3 at various pressures

and conduction bands plays a crucial role in the electronic arrangement. The peaks of Sr-4*p* and P-3*p* shift towards the fermi level while pressure is applied due to the hybridization with Cl-3p (Br-4p), supports the reduction of bandgap (E_g). Total Density of States (TDOS) gives a complete idea about the distribution of electronic states. In our investigation (as depicted in Fig. 12), a decline was noted in TDOS for both compounds when subjected to applied pressure. This decrease stems from the alteration in the E_g and structural compression induced by pressure which justifies the findings of PDOS.

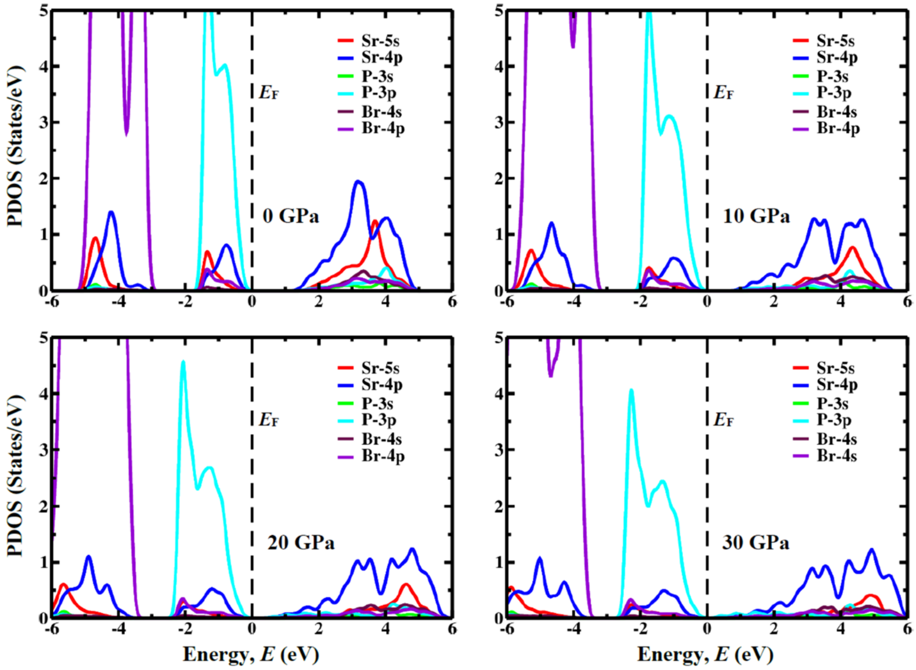

Fig. 11 The partial density of states of Sr_3PBr_3 at various pressures

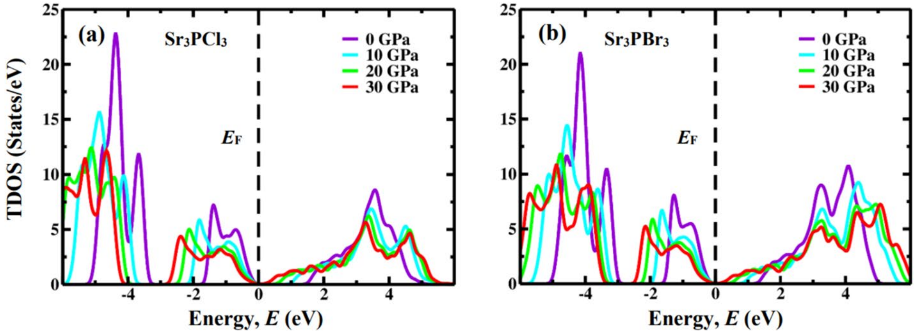

Fig. 12 The total density of states of Sr_3PX_3 (X = Cl, Br) at different pressures

Grasping these variations yields noteworthy discoveries on the electronic properties and features of the material, crucial for enhancing its efficacy across diverse applications.

The charge density describes the distribution of electronic charges within a given system. It helps to provide an initial prediction on the most dominant type of bonding present in the system. Electron charge density for both compounds at 0 GPa and 30 Gpa, is illustrated in Fig. 13. From the electron charge density, we can observe the real potential positions of the electrons. The right bar indicates the scale of the electron charge density, blue for low and red for high. Both compounds were found to have spherical forms under all pressures. This is an indication that the bond within the materials is highly likely to be

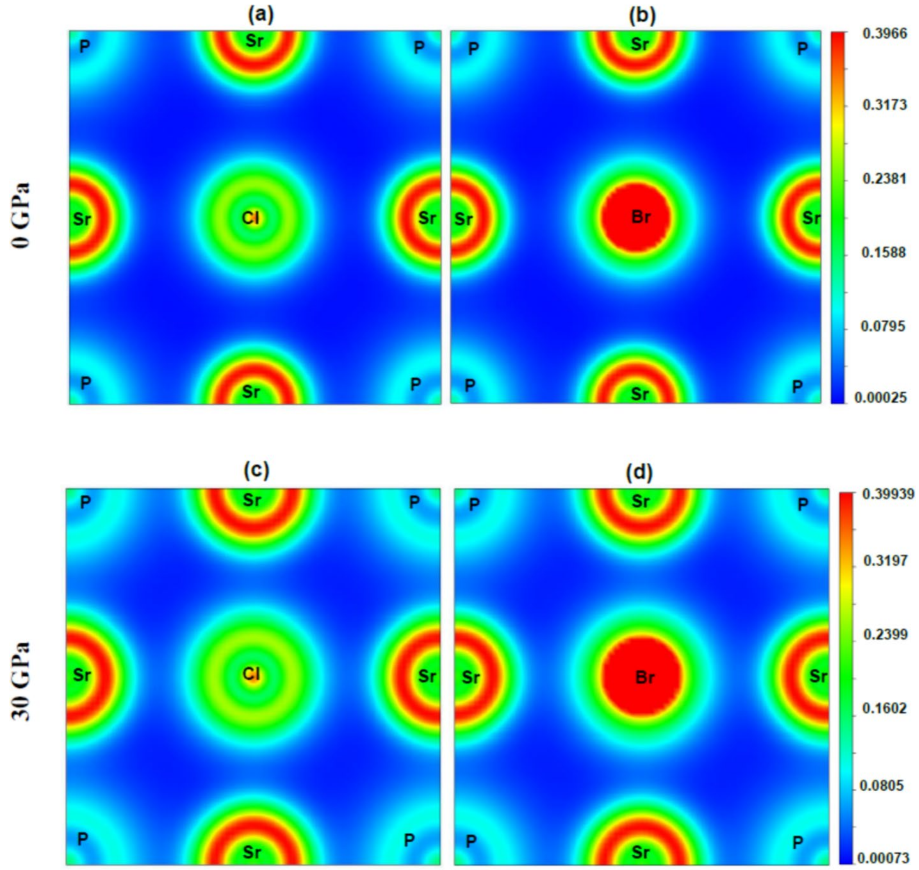

Fig. 13 Electron charge density distribution for Sr_3PX_3 at 0 and 30 GPa pressure

mostly ionic. However, a further analysis should be conducted, such as by using Bader charge analysis (Pitriana et al. 2019), if one wants to investigate the degree of the charge transfer between anions and cations in the materials. This is needed before a final conclusion is drawn about the type of bond present in the materials. With increased pressure, the density of electron charge did increase slightly, but not sufficiently to generate any hybridization or bonding.

Finally, effective mass was calculated to understand the charge carriers' motion under impact of pressure, depicted in Fig. 14 and Table 3. It helps to understand carrier mobility, Band Structure Analysis and transport properties. Effective mass is calculated using this equation (Zhao et al. 2018b),

$$m^* = \hbar^2 \left[\frac{\partial^2 \varepsilon(k)}{\partial k^2} \right]^{-1}$$

The effective mass was performed by taking the second derivative of the energy dispersion relation (E-k curve) with respect to momentum (k). The analyzed data showed an inverse

Fig. 14 Effective masses of Sr_3PX_3 (X = Cl, Br) at different pressures

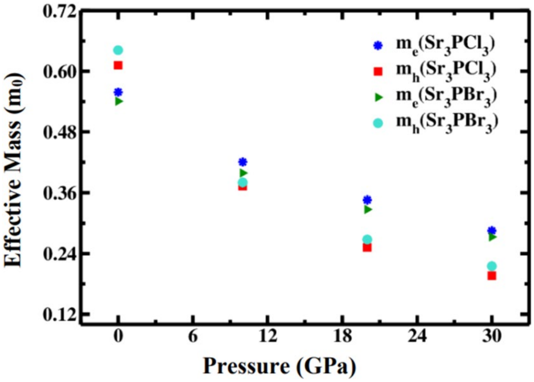

Table 3 Calculated effective masses of electron (m_e) and hole (m_h), and ratio of effective mass (D) of Sr_3PX_3 (X = Cl and Br) under various hydrostatic pressure. The masses are multiplications of rest mass of an electron $m_0 = 9.11 \times 10^{-31}$ kg

Pressure (GPa)	Sr_3PCl_3			Sr_3PBr_3		
	m_e	m_h	D	m_e	m_h	D
0	0.56	0.61	0.91	0.54	0.64	0.84
10	0.42	0.37	1.13	0.40	0.38	1.05
20	0.35	0.25	1.37	0.33	0.27	1.22
30	0.29	0.20	1.45	0.27	0.22	1.27

relation for both m_e and m_h with pressure. As we know carrier mobility has an inverse relationship with effective mass. While applying pressure, the effective mass of the electrons and holes was reduced, indicating high carrier mobility and charge carrier acceleration, which is advantageous in electronic and optoelectronic applications.

3.4 Mechanical properties

Elastic constants are crucial in establishing the mechanical characteristics of materials, since they dictate the response of a crystal to external forces (Husain et al. 2023a; Rahman et al. 2020). For cubic crystal materials, only three elastic constants are independent which are: C_{11}, $C_{12,}$ and C_{44} (Husain et al. 2023b). These three independent elastic constants of a compound are bound to follow a set of criteria if the compound is to be mechanically stable. These criteria, also known as Born stability criteria (Born 1940), are:

$$C_{11} > 0, C_{11} - C_{12} > 0, C_{11} + 2C_{12} > 0 \text{ and} C_{44} > 0$$

Sr_3PX_3 follows all four of these criteria. The Cauchy pressure (C_p), crystal stiffness (C_s) and Kleinman parameters (ζ) can be found using the three elastic constants. The equations from which they can be found are:

$$C_p = C_{12} - C_{44}$$

$$C_s = \frac{C_{11} - C_{12}}{2}$$

$$\zeta = \frac{C_{11} + 8C_{12}}{7C_{11} + 2C_{12}}$$

Cauchy pressure gives an idea of a compound's brittleness/ductility. Positive value means that the compound is ductile (Feng and Cui 2014). We can come to the conclusion whether Sr_3PX_3 is ductile or brittle once we also overviewed the Poisson's and Pugh's ratios. The ability of a compound to withstand shear deformation when shear stress is applied in the $[1\overline{1}0]$ direction on the (110) plane is the crystal stiffness which increases with pressure as shown in Table 4. The value of Kleinman parameter can be between 0 and 1. Values closer to 0 indicate an insignificant contribution to bond bending and the near 1 value indicates marginal contribution to bond stretching (Kleinman 1962). Pressure also has an effect as per Table 4. Here, the values also show almost similar results for Sr_3PBr_3 as (Ghosh et al. 2024a) found.

Table 5 consists of the following mechanical properties alongside the effects of pressure on them:

bulk modulus (*B*), shear modulus (*G*), Young's modulus (*Y*), Pugh's ratio (*B/G*), Poisson's ratio(ν), Machinability index (μ_M), Hardness factor (H_v). It is possible to estimate Bulk Modulus and Shear Modulus using the Voigt-Reuss-Hill method, where the Voigt's and Reuss's approximation of bulk moduli and then shear moduli are averaged (Gueddouh et al. 2016; Kleinman 1962):

$$B_V = \frac{1}{3}\left(C_{11} + 2C_{12}\right)$$

$$B_R = B_V = \frac{1}{3}\left(C_{11} + 2C_{12}\right)$$

$$B = \frac{1}{2}(B_V + B_R)$$

Here, B_V is the Voigt's bulk modulus, B_R is the Reuss' bulk modulus and *B* is the Hill's bulk modulus or simply bulk modulus.

Table 4 Calculated values of independent elastic constants C_{ij} (GPa) where ij = 11, 12 and 44, Cauchy Pressure (C_p), Crystal stiffness parameter (C_s) and Kleinman Factor (ζ) in Sr_3PX_3 (X = Cl. and Br) perovskites under various hydrostatic pressures

Pressure (GPa)	Compound	C_{11}	C_{12}	C_{44}	C_p	C_s	ζ
0	Sr_3PCl_3	76.31	7.47	16.24	− 8.76	34.42	0.247
	Sr_3PBr_3	70.75	7.20	14.17	− 6.97	31.78	0.251
	Sr_3PBr_3 (Ghosh et al. 2024a)	69.99	9.26	14.65	–	–	–
10	Sr_3PCl_3	173.41	16.58	13.69	2.89	78.41	0.245
	Sr_3PBr_3	173.20	16.23	11.57	4.66	78.49	0.243
20	Sr_3PCl_3	259.43	24.65	9.32	15.33	117.39	0.244
	Sr_3PBr_3	259.64	24.00	7.66	16.34	117.82	0.242
30	Sr_3PCl_3	338.36	31.78	3.94	27.84	153.29	0.243
	Sr_3PBr_3	338.77	31.20	2.95	28.25	153.79	0.241

Table 5 Calculated Bulk modulus (B), Young's modulus (Y), Shear modulus (G), Pugh's ratio (B/G_H), Poisson's ratio (ν), machinability index (μ_M), hardness factor (H_ν), and Zener anisotropy (A) for Sr_3PX_3 (X = Cl and Br) under various pressure

Pressure (GPa)	Compound	B (GPa)	Y (GPa)	G (GPa)	μ_M	H_ν	B/G	ν	A
0	Sr_3PCl_3	30.42	53.27	22.05	1.87	5.38	1.38	0.208	0.47
	Sr_3PBr_3	28.38	48.01	19.71	2.00	4.47	1.44	0.218	0.45
	Sr_3PBr_3 Ghosh et al. (2024))	29.50	48.35	19.70	–	–	1.50	–	–
10	Sr_3PCl_3	68.86	78.62	30.01	5.03	2.54	2.29	0.310	0.17
	Sr_3PBr_3	68.55	73.80	27.94	5.93	1.91	2.45	0.321	0.15
20	Sr_3PCl_3	102.91	91.03	33.65	11.04	1.23	3.06	0.353	0.08
	Sr_3PBr_3	102.55	86.90	31.98	13.39	0.88	3.21	0.359	0.07
30	Sr_3PCl_3	133.97	96.76	35.07	34.01	0.34	3.82	0.380	0.03
	Sr_3PBr_3	133.72	94.21	34.07	45.34	0.18	3.93	0.383	0.02

$$G_V = \frac{1}{5}(C_{11} - C_{12} + 3C_{44})$$

$$G_R = \frac{5C_{44}(C_{11} - C_{12})}{4C_{44} + 3\left(C_{11} - C_{12}\right)}$$

$$G = \frac{1}{2}(G_V + G_R)$$

Similarly, G_V is the Voigt's shear modulus, G_R is the Reuss' shear modulus and G is the Hill's shear modulus or simply shear modulus.

Bulk and shear moduli indicate resistance to fracture and ability to resist shear stress respectively. It can be concluded from Table 5 that Sr_3PCl_3 has higher fracture resistance and plastically deforms better than Sr_3PBr_3 as Sr_3PCl_3 has high bulk modulus and shear modulus (30.42 GPa and 22.05 GPa compared to 28.38 GPa and 19.71 GPa of Sr_3PBr_3 at ambient pressure). This comparison stays the same at higher pressure. Based on the bulk and shear modulus values, Young's modulus can be calculated. The correlation among shear modulus, bulk modulus, and Young's modulus is (Wang et al. 2015):

$$Y = \frac{9BG}{3B + G}$$

Young's modulus of Sr_3PCl_3 is higher than Sr_3PBr_3 across all pressure points. At 0 GPa, Young's modulus of Sr_3PCl_3 is 53.27 GPa and Sr_3PBr_3 is 48.01 GPa which means Sr_3PCl_3 stiffer compared to Sr_3PBr_3.

Machinability indicates how easy it is for a material to be cut (machined). High machinability also means less tool wear. Machinability can be measured by a machinability index (μ_M) (Sun et al. 2005):

$$\mu_M = \frac{B}{C_{44}}$$

Both compounds have low machinability. However, the machinability index grows rapidly with increasing pressure. At 30 GPa pressure, the machinability index of Sr_3PCl_3 becomes 34.01 and the machinability index of Sr_3PBr_3 becomes 45.34. To note, increasing pressure not only increases mechanical performance of these materials but also increases their machinability.

Hardness can be used to understand a materials' elastic and plastic properties. Hard materials tend to be brittle in nature but also more wear resistant. Hardness can be measured from following equation (Al-Fahdi et al. 2021):

$$H = 2\left(K^2 G\right)^{0.585} - 3;\ K = {}^{G}\!/_{B}$$

The hardness for Sr_3PCl_3 was found to be 5.38 GPa and for Sr_3PBr_3 it is 4.47 GPa. Sr_3PCl_3 was harder compared to Sr_3PBr_3 at ambient pressure but increasing pressure reduces the hardness rapidly for both compounds.

Poisson and Pugh's ratio are two important parameters to determine a material's brittleness/ductility alongside Cauchy pressure. Poisson's ratio can be determined by the following equation:

$$\mathrm{v} = \frac{(3\mathrm{B} - 2\mathrm{G})}{2\,(3\mathrm{B} + \mathrm{G})}$$

Pugh's ratio is a simple analogy of shear and bulk moduli (*B*/*G*). There is a critical value of 0.26 for Poisson's ratio and 1.75 for Pugh's ratio (Al-Fahdi et al. 2021; Pugh 1954; Vaitheeswaran et al. 2007). When the value exceeds the critical threshold, the material exhibits ductility, while falling below it results in brittleness (Ayaz et al. 2021; Khattak et al. 2022). Poisson's ratio and Pugh's ratio Sr_3PCl_3 and Sr_3PBr_3 is illustrated in Fig. 15 with variation of pressure. Both Sr_3PCl_3 and Sr_3PBr_3 compounds were found to be brittle in normal condition. At 10 GPa pressure, they become ductile, and as the pressure rises, so does their ductility. A similar transformation has also been observed in compounds like Sr_3AsCl_3 and Sr_3SbCl_3 (Hosen 2024).

Zener anisotropy factor also known as Zener ratio is the quantitative value that determines a material's deviation from isotropy and is expressed as,

$$A = \frac{2C_{44}}{C_{11} - C_{12}}$$

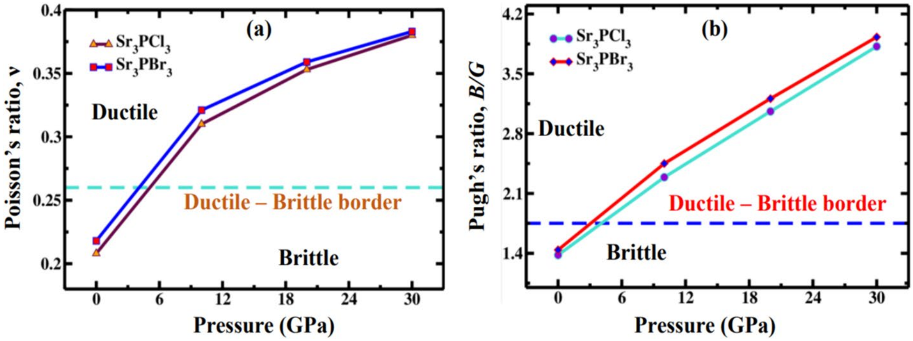

Fig. 15 Calculated **a** Poisson's ratio, **b** Pugh's ratio for Sr_3PX_3 (X = Cl, Br) at various applied pressures

Zener ratio of 1 indicates a material being perfectly isotropic. While values farther from 1 determine anisotropy of varying magnitude, dependent on the deviation of the value itself. As per Table 5, both of the materials are found to be anisotropic at ambient temperature. Anisotropy increases rapidly when increasing pressure is applied. This can be visualized with different 3D anisotropy graphs in Fig. 16. A shift from the spherical form signifies anisotropy. Poisson's ratio, Young's modulus, and shear modulus are all found to be anisotropic in 0 GPa and become extremely anisotropic in 30 GPa,

Debye temperature can describe various phenomena related to solid-state physics. It can be determined by the following equation (Sun et al. 2005):

$$\Theta_D = \frac{h}{k_B}\left[\frac{3n}{4\pi}\left(\frac{N_A\rho}{M}\right)\right]^{\frac{1}{3}} v_m$$

Here, Θ_D = Debye temperature, h = Planck's constant, n = number of atoms in a unit cell, k_B = Boltzmann's constant, ρ = density, N_A = Avogadro's number, M = molecular weight, v_m (m/s) = average sound velocity.

(a) Young's Modulus

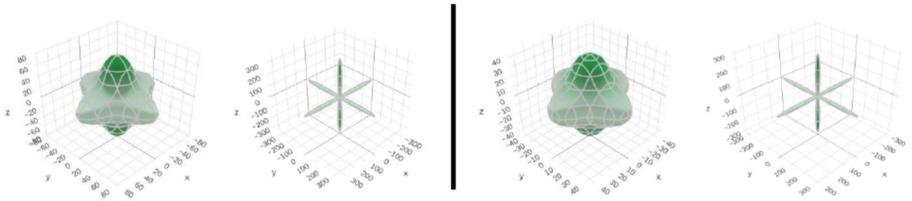

(b) Shear Modulus

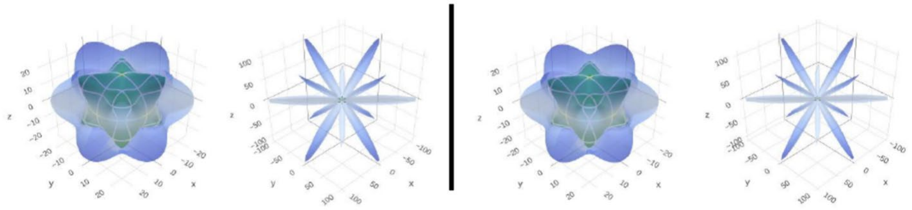

(c) Poisson's Ratio

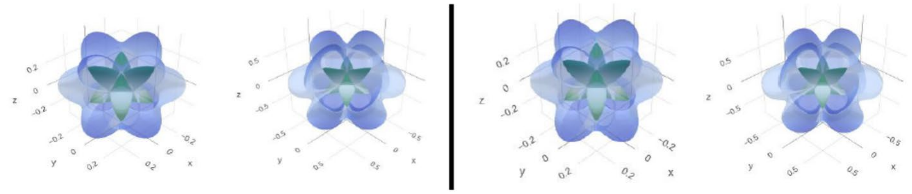

Fig. 16 3D structure of Sr_3PX_3 (X = Cl, Br) at 0 GPa and 30 GPa

v_m can be determined by following set of equations: (where, v_s(m/s) = shear sound velocity and v_l(m/s) = longitudinal sound velocity)

$$\mathrm{v_m} = \left[\frac{1}{3}\left(\frac{2}{\mathrm{v_s}^3}+\frac{1}{\mathrm{v_l}^3}\right)\right]^{-1/3}$$

$$\mathrm{v_s} = \sqrt{\frac{\mathrm{G}}{\rho}}$$

$$v_l = \sqrt{\frac{3B+4G}{3\rho}}$$

The sound velocities, Debye temperature and melting temperature are listened to Table 6. At 0 GPa pressure, Debye temperature of Sr_3PCl_3 is 282.07 K and Debye temperature of Sr_3PBr_3 234.29 K. This value rises for both compounds as pressure increases. Under ambient pressure, the melting points of Sr_3PCl_3 and Sr_3PBr_3 are 1004.02 K and 971.13 K, respectively. This suggests both compounds to withstand their structural integrity at high temperatures,

3.5 Optical properties

Understanding a compound's optical essentials in figuring out its possible applications in photovoltaic and optoelectronic systems (Rasheduzzaman et al. 2021). Researchers have developed an interest in lead-free, non-toxic, narrow band gap halides due to their remarkable optical characteristics. Reducing the band gap can be achieved quickly and simply by applying hydrostatic pressure (Hossain et al. 2021c; Islam et al. 2021a). To get the right details regarding a material's compatibility and boost device efficiency, optical function research is essential. For that, the optical functions of refractive index, dielectric function, absorption, conduction, extinction coefficient, loss function, and reflectivity of under induced pressures between 0 and 30 GPa for Sr_3PX_3 (X = Cl, Br) are explored.

The dielectric function is a crucial optical property that regulates the rate of charge-carrier recombination (Liu et al. 2018). It presents an understandable image of how optoelectronic devices function, that is employed to investigate how photons and electrons interact

Table 6 Calculated values of shear sound velocity v_s(m/s), longitudinal sound velocity v_l(m/s), average sound velocity v_m(m/s), Debye temperature Θ_D(K) and melting temperature T_m (K) for Sr_3PX_3 (X = Cl, Br) under various hydrostatic pressures

Pressure		0 GPa	10 GPa	20 GPa	30 GPa
Sr_3PCl_3	v_s	2710.58	2868.90	2872.97	2816.39
	v_l	4464.63	5464.19	6020.50	6393.76
	v_m	2995.06	3208.47	3231.23	3179.30
	Θ_D	282.07	322.44	337.04	340.70
	T_m	1004.02	1577.85	2086.24	2552.74
Sr_3PBr_3	v_s	2309.13	2480.49	2509.55	2488.51
	v_l	3845.57	4826.81	5347.15	5706.46
	v_m	2554.27	2777.98	2824.86	2810.31
	Θ_D	234.29	272.93	288.05	294.32
	T_m	971.13	1576.63	2087.46	2555.15

(Murnaghan 1937). Figure 17a and b shows a dielectric constant of Sr_3PX_3 (X = Cl, Br) which have two parts (Real and Imaginary). Dielectric constant of a material is calculated by this equation,

Here, $\varepsilon_1(\omega)$ represents real part and $\varepsilon_2(\omega)$ represent imaginary parts respectively. It is clearly apparent from the part of the dielectric functions that is consistent in between the patterns in the spectra of the two materials. Moreover, both Sr_3PCl_3 and Sr_3PBr_3 structures exhibit a higher peak in their dielectric constants, with the shift happening at lower photon energies (redshift) as a result of the bandgap being lower as pressure rises. As a consequence of these transformations, under 30 GPa of pressure, it is expected that the researched compounds will capture visible light energy for photovoltaic conversion, as shown in Fig. 17a, which could potentially enhance the efficiency of solar cells. Imaging systems, structural monitoring, and applications that are sensitive to pressure would benefit greatly from this redshift (Hossain et al. 2021c). The static dielectric function (Fig. 17a) of the studied materials at 30 GPa is considerably higher than that at lower pressure. This implies that the two materials will exhibit their best optoelectronic properties at 30 GPa as materials with larger static dielectric function generally possess better optoelectronic performance (Liu et al. 2018). This is because materials with larger $\varepsilon_1(0)$ values tend to possess a lower charge recombination (Hosen et al. 2024b), making them favorable for optoelectronic applications. As seen from Fig. 17a and b, the two compounds' dielectric functions' maximum peaks for the real and imaginary portions at 30 GPa are significantly higher in the visible region than those at lower hydrostatic pressure. These results clearly imply that at 30 GPa, the two materials are predicted to possess the best optical properties at visible energy region. In order to analyze optical transitions between the valence and conduction bands, understanding the imaginary component of the dielectric function $\varepsilon_2(\omega)$ is crucial. The material's band gap and optical absorption are also connected to the

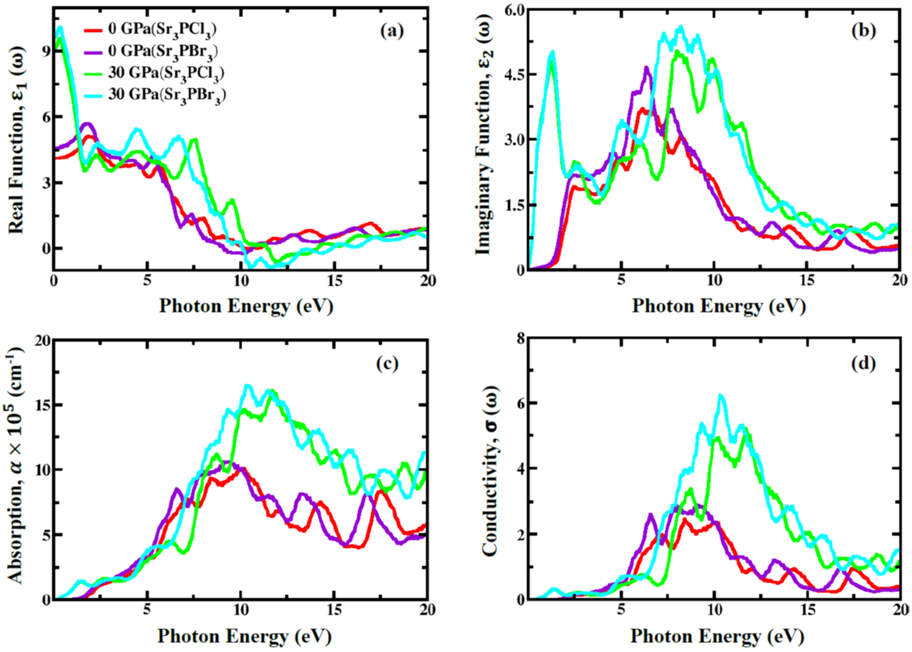

Fig. 17 Measured **a** dielectric function (real part), **b** dielectric function (imaginary), **c** absorption, **d** conductivity for Sr_3PX_3 (X = Cl, Br) at 0 GPa and 30 GPa

$\varepsilon_2(\omega)$. In the visible range, the applied pressure raises $\varepsilon_2(\omega)$, analogous to optical absorption. The peaks also transport a region with low photon energy (redshift), indicating that these compounds are effective visible light absorbers under pressure.

One of the many optical properties used to evaluate the performance of solar cells is the absorption coefficient (Islam et al. 2021b). The optical absorption coefficient (α) measures the capacity to absorb light energy, which offers key insights into the effectiveness of solar energy transformation (Islam et al. 2021a). Figure 17c shows the absorption coefficient of Sr_3PX_3 (X=Cl, Br) in different pressure levels between 0 and 20 eV energy levels. From the figures, it is clear that the transfer of charges between VB and CB occurs at the band gap as an outcome of the absorption of ultraviolet radiation at 0 GPa. The primary absorption shifts from the electromagnetic spectrum's ultraviolet to a visible range in response to pressure increase, which is constant with a band gap variation that is pressure-dependent (Hossain et al. 2021c; Islam et al. 2021a; Kholil and Bhuiyan 2021). This is an indication of this material's better absorptivity of light.

When light with energy exceeding the band gap hits a material, it can excite electrons within the valence band to conduction band. Therefore, with more holes in the valence band and electrons in the conduction band, the material's conductivity increases. This can be calculated with the equation (Shah et al. 2023),

$$\sigma(\omega) = \frac{\alpha(\omega)n(\omega)c}{4\pi}$$

The optical conductivity for Sr_3PX_3 (X=Cl, Br) is illustrated in Fig. 17d, it shows a similar property like other optical properties. Rarely any peaks were found in low-energy regions. There is a distinguishing peak difference between Sr_3PCl_3 and Sr_3PBr_3, where Sr_3PBr_3 shows more conductivity. Moreover, with applied pressure, the conductivity also increased for both compounds with redshift. This further supports our initial proposal for utilizing this pressurized application.

The energy of light reflected from the surface of the Sr_3PX_3 can be used to determine its surface nature (Roknuzzaman et al. 2017). Figure 18a displays reflectivity, $R(\omega)$, which is calculated from dielectric function and shown between the energies of 0 and 20 eV. Reflectivity, R is calculated from this relation (Ayub et al. 2024; Mahmud et al. 2024),

$$R(\omega) = \frac{(n-1)^2 + k^2}{(n+1)^2 + \mathrm{k}^2}$$

From the figures, we see that the visible range reflectivity (R) of Sr_3PX_3 (X=Cl, Br) increases significantly when pressure rises from 0 to 30 GPa. Plots of $\varepsilon_2(\omega)$ demonstrate that the highest reflectivity values correlate to the energy range where materials absorb the most. The higher reflectivity value when stressed in high-energy zones suggests the material under the study would be more efficient in preventing solar heating.

Figure 18b shows the extinction coefficient of Sr_3PX_3 (X=Cl, Br) which is highly associated with the static part, $\varepsilon_1(\omega)$ of dielectric function and expressed as (Mahmud et al. 2024; Shah et al. 2023),

$$k(\omega) = \left[\frac{\left\{\varepsilon_1^2(\omega) + \varepsilon_2^2(\omega)\right\}^{\frac{1}{2}} - \varepsilon_1(\omega)}{2}\right]^{\frac{1}{2}}$$

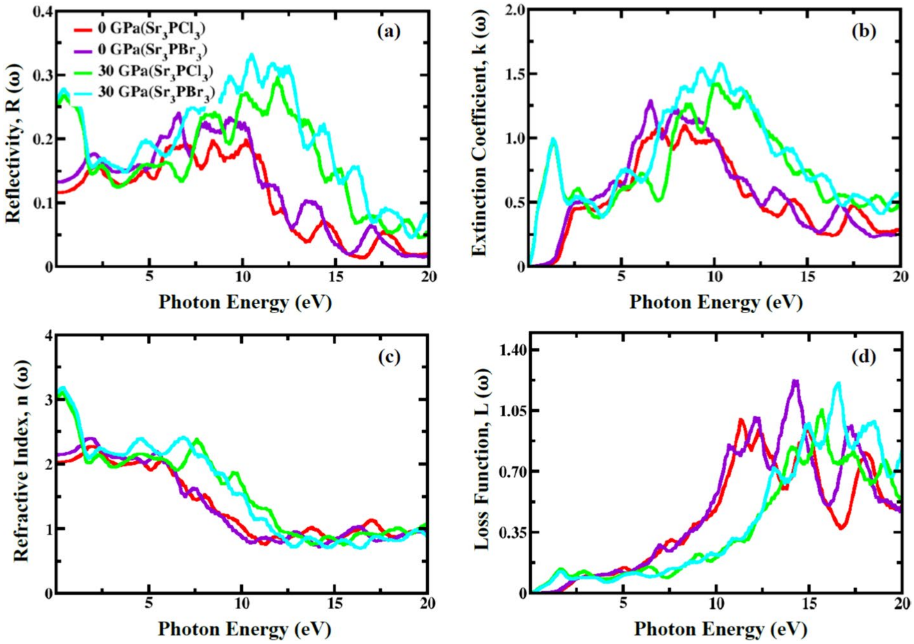

Fig. 18 Measured **a** reflectivity, **b** extinction coefficient, **c** refractive index and **d** loss function for Sr_3PX_3 (X = Cl, Br) at 0 GPa and 30 GPa

With increasing pressure extinction coefficient curve goes to the higher energy regions (redshift). Raising extinction coefficient means raising the rate at which a substance absorbs or scatters light as it passes through. This can result in diminished light transmission through the substance, causing objects to appear darker or less visible. In practice, a larger extinction coefficient might reduce the visibility or transparency of materials such as optics and environmental monitoring.

Figure 18c displays refractive index, $n(\omega)$ of Sr_3PX_3. This equation gives the refractive index (n) (Ayub et al. 2024; Mahmud et al. 2024),

$$n(\omega) = \left[\frac{\{\sqrt{\varepsilon_1^2(\omega) + \varepsilon_2^2(\omega)}\} + \varepsilon_1(\omega)}{2} \right]^{\frac{1}{2}}$$

From the figures it shows that, as pressure rises, $n(0)$ also begins to ascend, which suits both compounds for optoelectronic application. The refractive index is an important metric for measuring the degree of light refraction, especially in photoelectric applications. Photons are slowed by electron interactions while entering a substance, resulting in a refractive index of $n(\omega)$ is more than one. The more photons that are slowed down as they pass through a substance, the higher its refractive index.

The electron loss function is the measure of the energy that electrons lose when moving through a dielectric substrate. When photons are produced that have greater energy than the bandgap of the substance, energy is dissipated in Sr_3PX_3 (X = Cl, Br), as shown by the peak in the plot of $L(\omega)$ in Fig. 18d. The following formula is used to calculate the electron loss function (Mahmud et al. 2024; Shah et al. 2023),

$L(\omega) = \tau(\frac{-1}{\varepsilon(\omega)})$

This figure shows that the energy range of 8 ~ 10 eV, where $L(\omega)$ peaks regarding the cubic structure of Sr_3PX_3. For optical photon spectra and infrared spectra, Since $L(\omega)$ peaks appear infrequently below 2 eV, Sr_3PX_3 could serve as an efficient optical absorption layer. The results show that a significant redshift is caused by increased pressure, indicating an enhancement in optical loss and photon energy for all structures. When developing and optimizing these materials for designated purpose, the loss function of Sr_3PX_3 should be carefully taken into account as it plays a significant influence on its overall performance.

4 Conclusion

Both compounds maintain mechanical stability across all pressures, as indicated by the Born stability analysis. They also maintain dynamic stability, as evidenced by the positive values in the phonon dispersion curves. The size of Sr_3PCl_3 exceeds that of Sr_3PBr_3 due to the larger size of bromine. As pressure is applied, the volume, lattice parameter, and bond length decrease for both compounds. As for electronic properties, both Sr_3PCl_3 and Sr_3PBr_3 showed pretty much similar properties. The band gap measured at 30 GPa was 0.22 eV and 0.21 eV using GGA-PBE, while with TB-mBJ, it was 1.07 eV and 0.92 eV, respectively, indicating a relatively low value at this pressure. The density of states revealed a decrease in energy levels with pressure. Effective mass of m_e and m_h also decreased with increased pressure. No hybridization or overlapping were found from the electron charge density. Bulk modulus, Young's modulus, shear modulus, Poisson's ratio, and Pugh's ratio demonstrate improvements for Sr_3PCl_3 However, the machinability was found to be better for Sr_3PBr_3. Increased pressure shifted the brittle nature of both compounds to ductile which further increases with applied pressure. The Debye temperature and melting temperatures justify their application in a harsh temperature environment. For optical properties, a redshift was observed as the spectral lines shifted towards the lower energy side. Absorption increased with the rise in pressure, while reflection decreased in the visible range, indicating favorable characteristics for optoelectronic applications. In terms of the loss function, there was no increase observed until a certain threshold. This research aligns with previous research on Sr_3PBr_3, with the only notable difference being a slight variation in the lattice parameter. The objective of reducing the band gap and improving optoelectronic and other properties through induced pressure has been achieved successfully. Since this research is simulation-based, there may be some irregularities and discrepancies compared to real-life applications.

Author contribution S.J.: Investigation, methodology, data curation, writing the original, draft reviewing and editing. M.A.H.: Formal analysis, software, calculation and analysis, writing the original draft, reviewing and editing. M.A.Y.: Data curation, writing the original draft, reviewing and editing. M.M.H.: Data curation, writing the original draft, reviewing and editing. R.K.P.: Data curation, writing the original draft, reviewing and editing. N.F.A.M.: Formal analysis, software, data curation, reviewing and editing. M.S.A.J.: Formal analysis, software, data curation, reviewing and editing. A.A.M.: Formal analysis, software, data curation, reviewing and editing. A.H.: Investigation, conceptualization, software, methodology, data curation, calculation and analysis, writing the original draft, supervision, reviewing and editing.

Funding We did not receive any funding for this research.

Data availability No datasets were generated or analysed during the current study.

Declarations

Conflict of interest The authors declare no competing interests.

References

Ahmad, A.S., Su, Y., Liu, S.Y., Ståhl, K., Wu, Y.D., Hui, X.D., Ruett, U., Gutowski, O., Glazyrin, K., Liermann, H.P., Franz, H., Wang, H., Wang, X.D., Cao, Q.P., Zhang, D.X., Jiang, J.Z.: Structural stability of high entropy alloys under pressure and temperature. J. Appl. Phys. **121**, 235901 (2017). https://doi.org/10.1063/1.4984796

Al-Fahdi, M., Rodriguez, A., Ouyang, T., Hu, M.: High-Throughput computation of new carbon allotropes with diverse hybridization and ultrahigh hardness. Crystals **11**, 783 (2021). https://doi.org/10.3390/cryst11070783

Algahtani, A., RehmanLiaqat, F.M., Juraev, N., Khan, I., Alsuhaibani, A.M., AbdullahTirth, V., Refat, M.S., Zaman, A.: Probing the physical properties of Sr_3AsX_3 (X = F and Br) perovskite compounds for prospective solar cell applications employing the DFT framework. Inorganic Chem. Commun. **162**, 112186 (2024). https://doi.org/10.1016/j.inoche.2024.112186

Ali, A.H., Ahmed, A.M., Abdel-Khaliek, A.A., Abd El Khalik, S., Abass, S.M., Shaban, M., Rabia, M.: Preparation of inorganic lead-free CuO/Cs_2SnCl_6-KI perovskite for green hydrogen production from wastewater by using solar energy. J. Photochem. Photobiol. a: Chem. **445**, 115102 (2023). https://doi.org/10.1016/j.jphotochem.2023.115102

Ayaz, U., Shazia, A., Husain, M., Rahman, N., Bonyah, E.: Ab initio investigation of structural, electronic, magnetic, elastic, and optical properties of Cs-based chloro-perovskites $CsXCl_3$ (X = Be and Rh). AIP Adv. **11**, 105215 (2021). https://doi.org/10.1063/5.0065663

Ayub, G., Rahman, N., Husain, M., Sohail, M., Khan, R., Sfina, N., Elhadi, M., Azzouz-Rached, A., Alotaibi, A.: Tailoring the structural, elastic, electronic, and optical properties of Cs_2ScCuX_6 (X = Cl and F) double perovskite compounds via density functional theory (DFT). J. Phys. Chem. Solids **188**, 111942 (2024). https://doi.org/10.1016/j.jpcs.2024.111942

Babayigit, A., Duy Thanh, D., Ethirajan, A., Manca, J., Muller, M., Boyen, H.-G., Conings, B.: Assessing the toxicity of Pb- and Sn-based perovskite solar cells in model organism Danio rerio. Sci. Rep. **6**, 18721 (2016). https://doi.org/10.1038/srep18721

Bhalla, A.S., Guo, R., Roy, R.: The perovskite structure—a review of its role in ceramic science and technology. Mater. Res. Innovations **4**, 3–26 (2000). https://doi.org/10.1007/s100190000062

Blaha P., Schwarz K., Tran F., Laskowski R., Madsen G. K. H., Marks L. D.: WIEN2k: An APW+ lo program for calculating the properties of solids. J. Chem. Phys. 152, 074101 (2020). https://doi.org/10.1063/1.5143061

Born, M.: On the stability of crystal lattices. I. Math. Proc. Cambridge Philos. Soc. **36**, 160–172 (1940). https://doi.org/10.1017/S0305004100017138

Butt, M.K., Yaseen, M., Iqbal, J., Altowyan, A.S., Murtaza, A., Iqbal, M., Laref, A.: Structural, electronic, half–metallic ferromagnetic and optical properties of cubic $MAlO_3$ (M=Ce, Pr) perovskites: A DFT study. J. Phys. Chem. Solids **154**, 110084 (2021). https://doi.org/10.1016/j.jpcs.2021.110084

Dandia, A., Saini, P., Sharma, R., Parewa, V.: Visible light driven perovskite-based photocatalysts: A new candidate for green organic synthesis by photochemical protocol. Curr. Res.green Sustain. Chem. **3**, 100031 (2020). https://doi.org/10.1016/j.crgsc.2020.100031

Eperon, G.E., Habisreutinger, S.N., Leijtens, T., Bruijnaers, B.J., van Franeker, J.J., deQuilettes, D.W., Pathak, S., Sutton, R.J., Grancini, G., Ginger, D.S., Janssen, R.A.J., Petrozza, A., Snaith, H.J.: The importance of moisture in hybrid lead halide perovskite thin film fabrication. ACS Nano **9**, 9380–9393 (2015). https://doi.org/10.1021/acsnano.5b03626

Faridi, M.A., Tariq, S., Imran Jamil, M., Batool, A., Nadeem, S., Amin, A.: Pressure induced band-gap tuning in $KNbO_3$ for piezoelectric applications: quantum DFT-GGA approach. Chin. J. Phys. **56**, 1481–1487 (2018). https://doi.org/10.1016/j.cjph.2018.06.003

Feng, H.-J., Zhang, Q.: Predicting efficiencies >25% A_3MX_3 photovoltaic materials and Cu ion implantation modification. Appl. Phys. Lett. **118**, 111902 (2021). https://doi.org/10.1063/5.0039936

Feng, W., Cui, S.: Mechanical and electronic properties of Ti_2AlN and Ti_4AlN_3: a first-principles study. Can. J. Phys. **92**, 1652–1657 (2014). https://doi.org/10.1139/cjp-2013-0746

Filip, M.R., Giustino, F.: The geometric blueprint of perovskites. Proc. Natl. Acad. Sci. u.s.a. **115**, 5397–5402 (2018). https://doi.org/10.1073/pnas.1719179115

Fischer, T.H., Almlof, J.: General methods for geometry and wave function optimization. J. Phys. Chem. (2002). https://doi.org/10.1021/j100203a036

Gaillac, R., Pullumbi, P., Coudert, F.-X.: ELATE: an open-source online application for analysis and visualization of elastic tensors. J. Phys. Condens. Matter **28**(27), 275201 (2016). https://doi.org/10.1088/0953-8984/28/27/275201

Gao, J., Zeng, W., Tang, B., Fan, D.-H., Liu, Q.-J., Chang, X.-H., Zhong, M.: Effects of pressure on structural, mechanical, and electronic properties of trigonal and monoclinic $MgSiO_3$. Solid State Sci. **105**, 106261 (2020). https://doi.org/10.1016/j.solidstatesciences.2020.106261

Ghosh, A., Ahmed, F., Ferdous, M.J., Juhi, M.M.J., Buian, M.F.I., Miazee, A.A., Sajid, M., Maniruzzaman, M., Tighezza, A.M., Ahmmed, M.F., Islam, M.S.: Strain-induced changes in the electronic, optical and mechanical properties of the inorganic cubic halide perovskite Sr_3PBr_3 with FP-DFT. J. Phys. Chem. Solids **191**, 112053 (2024a). https://doi.org/10.1016/j.jpcs.2024.112053

Ghosh, A., Ferdous Rahman, Md., Kuddus, A., Mohammed, M.K.A., Rasidul Islam, Md., Bhattarai, S., Chaudhry, A.R., Irfan, A.: Investigating of novel inorganic cubic perovskites of A3BX3 (A=Ca, Sr, B P, As, X=I, Br) and their photovoltaic performance with efficiency over 28%. J. Alloys Comp. **986**, 174097 (2024b). https://doi.org/10.1016/j.jallcom.2024.174097

Ghosh, A., Rahman, M.F., Islam, M.R., Islam, M.S., Amami, M., Hossain, M.K., Md Ismail, A.B.: Inorganic novel cubic halide perovskite Sr_3AsI_3: Strain-activated electronic and optical properties. Heliyon **9**, e19271 (2023). https://doi.org/10.1016/j.heliyon.2023.e19271

Giannozzi, P., Baroni, S., Bonini, N., Calandra, M., Car, R., Cavazzoni, C., Ceresoli, D., Chiarotti, G.L., Cococcioni, M., Dabo, I., DalCorso, A., de Gironcoli, S., Fabris, S., Fratesi, G., Gebauer, R., Gerstmann, U., Gougoussis, C., Kokalj, A., Lazzeri, M., Martin-Samos, L., Marzari, N., Mauri, F., Mazzarello, R., Paolini, S., Pasquarello, A., Paulatto, L., Sbraccia, C., Scandolo, S., Sclauzero, G., Seitsonen, A.P., Smogunov, A., Umari, P., Wentzcovitch, R.M.: QUANTUM ESPRESSO: a modular and open-source software project for quantum simulations of materials. J. Phys. Condens. Matter **21**, 395502 (2009)

Gueddouh, A., Bentria, B., Lefkaier, I.K.: First-principle investigations of structure, elastic and bond hardness of Fe*x*B (*x*=1, 2, 3) under pressure. J. Magn. Magn. Mater. **406**, 192–199 (2016). https://doi.org/10.1016/j.jmmm.2016.01.013

Hosen, A.: Investigating the effects of hydrostatic pressure on the physical properties of cubic Sr_3BCl_3 (B = As, Sb) for improved optoelectronic applications: a DFT study. Heliyon (2024). https://doi.org/10.1016/j.heliyon.2024.e35855

Hosen, A., Hossain, Md.A., Abu-Jafar, M.S., Pingak, R.K., Mousa, A.A.: Unraveling lead-free Fr-based perovskites FrQCl3 (Q = Ca, Sr) and their pressure induced physical properties: DFT analysis for advancing optoelectronic performance. J.phys.chem.solids **193**, 112211 (2024a). https://doi.org/10.1016/j.jpcs.2024.112211

Hosen, A., Islam, M.R., Badhan, S.H.: Exploring the influence of pressure-induced semiconductor-to-metal transition on the physical properties of cubic perovskites $FrXCl_3$ (X = Ge and Sn). Heliyon (2024b). https://doi.org/10.1016/j.heliyon.2024.e27581

Hosen, A., Islam, M.R., Park, J.: Pressure-induced band gap shifting from ultra-violet to visible spectrum of non-toxic $RbCaBr_3$ cubic perovskite for enhancing optoelectronic applications. J. Inorg. Organomet. Polym. Mater. **34**, 1–10 (2024c)

Hossain, K.M., Hasan, Md.Z., Ali, Md.L.: Narrowing bandgap and enhanced mechanical and optoelectronic properties of perovskite halides: effects of metal doping. AIP Adv. **11**, 015052 (2021a). https://doi.org/10.1063/5.0039308

Hossain, K.M., Mitro, S.K., Hossain, Md.A., Modak, J.K., Rasheduzzaman, Md., Hasan, Md.Z.: Influence of antimony on the structural, electronic, mechanical, and anisotropic properties of cubic barium stannate. Mater. Today Commun. **26**, 101868 (2021b). https://doi.org/10.1016/j.mtcomm.2020.101868

Hossain, K.M., Zahid Hasan, Md., Lokman Ali, Md.: Understanding the influences of Mg doping on the physical properties of $SrMoO_3$ perovskite. Results Phys. **19**, 103337 (2020). https://doi.org/10.1016/j.rinp.2020.103337

Hossain, Md.S., Haque Babu, Md.M., Saha, T., Hossain, Md.S., Podder, J., Rana, Md.S., Barik, A., Rani, P.: Pressure induced semiconductor to metal phase transition in cubic $CsSnBr_3$ perovskite. AIP Adv. **11**, 055024 (2021c). https://doi.org/10.1063/5.0048979

Huang, Y., Zhang, T., Wang, J., Xu, S.-G., Zhang, P., Chen, S., Yin, W.-J., Zhang, X., Wei, S.-H.: Design of multifunctional quinternary metal-halide perovskite compounds based on cation-anion co-ordering. Chem. Mater. **32**, 5949–5957 (2020). https://doi.org/10.1021/acs.chemmater.0c00674

Husain, M., Rahman, N., Amami, M., Zaman, T., Sohail, M., Khan, R., Khan, A.A., Shah, S.A., KhanSaeedullah, A., ReshakAl-ShaalanAlharthiAlharthyAminTirth, A.H.N.H.S.S.A.M.A.V.: Predicting structural, optoelectronic and mechanical properties of germanium based $AGeF_3$ (A = Ga and In) halides perovskites using the DFT computational approach. Opt. Quant. Electron. **55**, 536 (2023a). https://doi.org/10.1007/s11082-023-04796-8

Husain, M., Rahman, N., Sfina, N., Al-Shaalan, N.H., Alharthi, S., Alharthy, S.A., Amin, M.A., Tirth, V., Khan, R., Sohail, M., Azzouz-Rached, A., Khattak, S.A., Khan, M.Y.: The comparative investigations of structural, optoelectronic, and mechanical properties of $AgBeX_3$ (X = F and Cl) metal halide-perovskites for prospective energy applications utilizing DFT approach. Opt. Quant. Electron. **55**, 920 (2023b). https://doi.org/10.1007/s11082-023-05187-9

Islam, M.A., Islam, J., Islam, M.N., Sen, S.K., Hossain, A.K.M.A.: Enhanced ductility and optoelectronic properties of environment-friendly $CsGeCl_3$ under pressure. AIP Adv. **11**, 045014 (2021a). https://doi.org/10.1063/5.0048849

Islam, M.A., Rahaman, Md.Z., Sen, S.K.: A comparative study of hydrostatic pressure treated environmentally friendly perovskites $CsXBr_3$ (X = Ge/Sn) for optoelectronic applications. AIP Adv. **11**, 075109 (2021b). https://doi.org/10.1063/5.0057287

Islam, Md.R., Zahid, A., Rahman, M.A., Rahman, Md.F., Islam, M.A., Hossain, M.K., Ali, M.A., Iqbal, M.A., Bakhsh, F.I., Ahmad, S.: Tuning the optical, electronic, and mechanical properties of inorganic Ca_3PCl_3 perovskite via biaxial strain. J.phys. Chem.solids **184**, 111722 (2024). https://doi.org/10.1016/j.jpcs.2023.111722

Jehan, A., Husain, M., Tirth, V., Algahtani, A., Uzair, M., Rahman, N., Khan, A., Khan, S.N.: Investigation of the structural, electronic, mechanical, and optical properties of $NaXCl_3$ (X= Be, Mg) using density functional theory. RSC Adv. **13**, 28395–28406 (2023)

Jiang, Q., Zhao, Y., Zhang, X., Yang, X., Chen, Y., Chu, Z., Ye, Q., Li, X., Yin, Z., You, J.: Surface passivation of perovskite film for efficient solar cells. Nat. Photonics **13**, 460–466 (2019). https://doi.org/10.1038/s41566-019-0398-2

Johnsson, M., Lemmens, P.: Crystallography and Chemistry of Perovskites. (2005). http://arxiv.org/abs/cond-mat/0506606

Jung, H.S., Park, N.-G.: Perovskite Solar Cells: From Materials to Devices. Small **11**, 10–25 (2015). https://doi.org/10.1002/smll.201402767

Kanhere, P., Chen, Z.: A review on visible Light active perovskite-based photocatalysts. Molecules **19**, 19995–20022 (2014). https://doi.org/10.3390/molecules191219995

Karsch, F., Patkós, A., Petreczky, P.: Screened perturbation theory. Phys. Lett. B **401**, 69–73 (1997). https://doi.org/10.1016/S0370-2693(97)00392-4

Khan, S.A., Khan, N.Z., Sohail, M., Runowski, M., Xu, X., Agathopoulos, S.: Recent developments of lead-free halide-perovskite nanocrystals: synthesis strategies, stability, challenges, and potential in optoelectronic applications. Mater. Today Phys. **34**, 101079 (2023)

Khattak, S.A., Abohashrh, M., Ahmad, I., Husain, M., Ullah, I., Zulfiqar, S., Rooh, G., Rahman, N., Khan, G., Khan, T., Salman Khan, M., Shah, S.K., Tirth, V.: Investigation of structural, mechanical, optoelectronic, and thermoelectric properties of $BaXF_3$ (X = Co, Ir) fluoro-perovskites: promising materials for optoelectronic and thermoelectric applications. ACS Omega **8**, 5274–5284 (2023). https://doi.org/10.1021/acsomega.2c05845

Khattak, S.A., Wabaidur, S.M., Islam, M.A., Husain, M., Ullah, I., Zulfiqar, S., Rooh, G., Rahman, N., Khan, M.S., Khan, G., Khan, T., Ghlamallah, B.: First-principles structural, elastic and optoelectronics study of sodium niobate and tantalate perovskites. Sci. Rep. **12**, 21700 (2022). https://doi.org/10.1038/s41598-022-26250-7

Kholil, M.I., Bhuiyan, M.T.H.: Effects of pressure on narrowing the band gap, visible light absorption, and semi-metallic transition of lead-free perovskite $CsSnBr_3$ for optoelectronic applications. J. Phys. Chem. Solids **154**, 110083 (2021). https://doi.org/10.1016/j.jpcs.2021.110083

Kleinman, L.: Deformation potentials in silicon I. Uniaxial Strain. Phys. Rev. **128**, 2614–2621 (1962). https://doi.org/10.1103/PhysRev.128.2614

Kohn, W., Sham, L.J.: Self-consistent equations including exchange and correlation effects. Phys. Rev. **140**, A1133–A1138 (1965). https://doi.org/10.1103/PhysRev.140.A1133

Kojima, A., Teshima, K., Shirai, Y., Miyasaka, T.: Organometal halide perovskites as visible-light sensitizers for photovoltaic cells. J. Am. Chem. Soc. **131**, 6050–6051 (2009). https://doi.org/10.1021/ja809598r

Kouchaksaraie, L.S.: Theoretical calculation of electrical and optical properties of $BaZrO_3$. Int. J. Math. Comput. Phys. Electr. Comput. Eng. **5**, 1680–1683 (2011)

Lan, Z., Meng, J., Zheng, K., Castelli, I.E.: Exploring the intrinsic point defects in cesium copper halides. J. Phys. Chem. C **125**, 1592–1598 (2021). https://doi.org/10.1021/acs.jpcc.0c11216

Langhoff, P.W., Epstein, S.T., Karplus, M.: Aspects of time-dependent perturbation theory. Rev. Mod. Phys. **44**, 602–644 (1972). https://doi.org/10.1103/RevModPhys.44.602

Lee, M.M., Teuscher, J., Miyasaka, T., Murakami, T.N., Snaith, H.J.: Efficient hybrid solar cells based on meso-superstructured organometal halide perovskites. Science **338**, 643–647 (2012). https://doi.org/10.1126/science.1228604

Liu, J., Li, N., Jia, J., Dong, J., Qiu, Z., Iqbal, S., Cao, B.: Perovskite films grown with green mixed anti-solvent for highly efficient solar cells with enhanced stability. Sol. Energy **181**, 285–292 (2019a). https://doi.org/10.1016/j.solener.2019.02.020

Liu, S.-C., Li, Z., Yang, Y., Wang, X., Chen, Y.-X., Xue, D.-J., Hu, J.-S.: Investigation of oxygen passivation for high-performance all-inorganic perovskite solar cells. J. Am. Chem. Soc. **141**, 18075–18082 (2019b). https://doi.org/10.1021/jacs.9b07182

Liu, X., Xie, B., Duan, C., Wang, Z., Fan, B., Zhang, K., Lin, B., Colberts, F.J.M., Ma, W., Janssen, R.A.J., Huang, F., Cao, Y.: A high dielectric constant non-fullerene acceptor for efficient bulk-heterojunction organic solar cells. J. Mater. Chem. A **6**, 395–403 (2018). https://doi.org/10.1039/C7TA10136H

Liu, Y.-Q., Wei, D., Cui, H.-L., Wang, D.-Q.: Photovoltaic effect related to methylammonium cation orientation and carrier transport properties in high-performance perovskite solar cells. ACS Appl. Mater. Interfaces **12**, 3563–3571 (2020). https://doi.org/10.1021/acsami.9b18452

Mahmud, S., Ali, M.A., Hossain, M.M., Uddin, M.M.: DFT aided prediction of phase stability, optoelectronic and thermoelectric properties of A_2AuScX_6 (A= Cs, Rb; X= Cl, Br, I) double perovskites for energy harvesting technology. Vacuum **221**, 112926 (2024)

Marshall, K.P., Walker, M., Walton, R.I., Hatton, R.A.: Enhanced stability and efficiency in hole-transport-layer-free $CsSnI_3$ perovskite photovoltaics. Nat. Energy **1**, 16178 (2016). https://doi.org/10.1038/nenergy.2016.178

Moghe, D., Wang, L., Traverse, C.J., Redoute, A., Sponseller, M., Brown, P.R., Bulović, V., Lunt, R.R.: All vapor-deposited lead-free doped $CsSnBr_3$ planar solar cells. Nano Energy **28**, 469–474 (2016). https://doi.org/10.1016/j.nanoen.2016.09.009

Murnaghan, F.D.: Finite deformations of an elastic solid. Am. J. Math. **59**, 235–260 (1937). https://doi.org/10.2307/2371405

Murnaghan, F.D.: The compressibility of media under extreme pressures. Proc. Natl. Acad. Sci. **30**, 244–247 (1944). https://doi.org/10.1073/pnas.30.9.244

Noel, N.K., Stranks, S.D., Abate, A., Wehrenfennig, C., Guarnera, S., Haghighirad, A.-A., Sadhanala, A., Eperon, G.E., Pathak, S.K., Johnston, M.B., Petrozza, A., Herz, L.M., Snaith, H.J.: Lead-free organic–inorganic tin halide perovskites for photovoltaic applications. Energy Environ. Sci. **7**, 3061–3068 (2014). https://doi.org/10.1039/C4EE01076K

Perdew, J.P., Burke, K., Ernzerhof, M.: Generalized gradient approximation made simple. Phys. Rev. Lett. **77**, 3865–3868 (1996). https://doi.org/10.1103/PhysRevLett.77.3865

Perdew, J.P., Chevary, J.A., Vosko, S.H., Jackson, K.A., Pederson, M.R., Singh, D.J., Fiolhais, C.: Atoms, molecules, solids, and surfaces: applications of the generalized gradient approximation for exchange and correlation. Phys. Rev. B **46**, 6671–6687 (1992). https://doi.org/10.1103/PhysRevB.46.6671

Pitriana, P., Wungu, T.D.K., Hidayat, R.: The characteristics of band structures and crystal binding in all-inorganic perovskite $APbBr_3$ studied by the first principle calculations using the density functional theory (DFT) method. Results Phys. **15**, 102592 (2019). https://doi.org/10.1016/j.rinp.2019.102592

Pugh, S.F.: XCII. Relations between the elastic moduli and the plastic properties of polycrystalline pure metals. London, Edinburgh, and Dublin Philos. Mag. J. Sci. **45**, 823–843 (1954). https://doi.org/10.1080/14786440808520496

Rahman, N., Husain, M., Yang, J., Murtaza, G., Sajjad, M., Habib, A., Karim, A., HaqZulfiqar, M.U., Rauf, A.: First principle study of structural, electronic, elastic, and magnetic properties of half-Heusler compounds ScTiX (X= Si, Ge, Pb, In, Sb, and Tl). J. Superconductivity Novel Mag. **33**, 3915–3922 (2020)

Rasheduzzaman, Md., Hossain, K.M., Mitro, S.K., Hadi, M.A., Modak, J.K., Hasan, Md.Z.: Structural, mechanical, thermal, and optical properties of inverse-Heusler alloys Cr_2CoZ (Z = Al, In): a first-principles investigation. Phys. Lett. A **385**, 126967 (2021). https://doi.org/10.1016/j.physleta.2020.126967

Ren, M., Qian, X., Chen, Y., Wang, T., Zhao, Y.: Potential lead toxicity and leakage issues on lead halide perovskite photovoltaics. J. Hazard. Mater. **426**, 127848 (2022)

Roknuzzaman, M., Ostrikov, K., Wang, H., Du, A., Tesfamichael, T.: Towards lead-free perovskite photovoltaics and optoelectronics by ab-initio simulations. Sci. Rep. **7**, 14025 (2017). https://doi.org/10.1038/s41598-017-13172-y

Seo, J., Noh, J.H., Seok, S.I.: Rational strategies for efficient perovskite solar cells. Acc. Chem. Res. **49**, 562–572 (2016). https://doi.org/10.1021/acs.accounts.5b00444

Shah, S.Z.A., Niaz, S., Nasir, T., Sifuna, J.: First principles insight into band gap tuning in bismuth based double perovskites $X_2NaBiCl_6$ (X= Cs, Rb, K) for enhanced optoelectronic and thermoelectric properties. Results Chem. **5**, 100828 (2023)

Stoumpos, C.C., Malliakas, C.D., Kanatzidis, M.G.: Semiconducting tin and lead iodide perovskites with organic cations: phase transitions, high mobilities, and near-infrared photoluminescent properties. Inorg. Chem. **52**, 9019–9038 (2013). https://doi.org/10.1021/ic401215x

Sun, Z., Music, D., Ahuja, R., Schneider, J.M.: Electronic origin of shearing in M2AC (M = Ti, V, Cr, A = Al, Ga). J. Phys. Condens. Matter **17**, 7169 (2005). https://doi.org/10.1088/0953-8984/17/46/001

Tian, S., Li, J., Li, S., Bu, T., Mo, Y., Wang, S., Li, W., Huang, F.: A facile green solvent engineering for up-scaling perovskite solar cell modules. Sol. Energy **183**, 386–391 (2019). https://doi.org/10.1016/j.solener.2019.03.038

Tran, F., Blaha, P.: Accurate band gaps of semiconductors and insulators with a semilocal exchange-correlation potential. Phys. Rev. Lett. **102**, 226401 (2009). https://doi.org/10.1103/PhysRevLett.102.226401

Vaitheeswaran, G., Kanchana, V., Svane, A., Delin, A.: Elastic properties of $MgCNi_3$—a superconducting perovskite. J. Phys. Condens. Matter **19**, 326214 (2007). https://doi.org/10.1088/0953-8984/19/32/326214

Vanderbilt, D.: Soft self-consistent pseudopotentials in a generalized eigenvalue formalism. Phys. Rev. B **41**, 7892–7895 (1990). https://doi.org/10.1103/PhysRevB.41.7892

Verma, A.S., Jindal, V.K.: Lattice constant of cubic perovskites. J. Alloy. Compd. **485**, 514–518 (2009)

Wang, L., Kutana, A., Zou, X., Yakobson, B.I.: Electro-mechanical anisotropy of phosphorene. Nanoscale **7**, 9746–9751 (2015). https://doi.org/10.1039/C5NR00355E

Wehrenfennig, C., Eperon, G.E., Johnston, M.B., Snaith, H.J., Herz, L.M.: High charge carrier mobilities and lifetimes in organolead trihalide perovskites. Adv. Mater. (Deerfield Beach, Fla.) **26**, 1584 (2014)

Wu, T., Qin, Z., Wang, Y., Wu, Y., Chen, W., Zhang, S., Cai, M., Dai, S., Zhang, J., Liu, J., Zhou, Z., Liu, X., Segawa, H., Tan, H., Tang, Q., Fang, J., Li, Y., Ding, L., Ning, Z., Qi, Y., Zhang, Y., Han, L.: The main progress of perovskite solar cells in 2020–2021. Nano-Micro. Lett. **13**, 152 (2021). https://doi.org/10.1007/s40820-021-00672-w

Xiong, R., Die, D., Xiao, L., Xu, Y.-G., Shen, X.-Y.: Probing the structural, electronic, and magnetic properties of AgnV (n = 1–12) clusters. Nanoscale Res. Lett. **12**, 625 (2017). https://doi.org/10.1186/s11671-017-2394-0

Yang, X., Wang, W., Ran, R., Zhou, W., Shao, Z.: Recent advances in $Cs_2AgBiBr_6$-based halide double perovskites as lead-free and inorganic light absorbers for perovskite solar cells. Energy Fuels **34**, 10513–10528 (2020). https://doi.org/10.1021/acs.energyfuels.0c02236

Yin, W.-J., Shi, T., Yan, Y.: Unique properties of halide perovskites as possible origins of the superior solar cell performance. Adv. Mater. **26**, 4653–4658 (2014). https://doi.org/10.1002/adma.201306281

Zhang, W., Eperon, G.E., Snaith, H.J.: Metal halide perovskites for energy applications. Nat. Energy **1**, 1–8 (2016). https://doi.org/10.1038/nenergy.2016.48

Zhao, X., Xiang, C., Huang, M., Ding, M., Jia, C., Jia, C., Sun, L., Sun, L.: Quantum dot solar cells. In: Emerging Photovoltaic Materials, pp. 611–658. John Wiley, Hoboken (2018a)

Zhao, Y.-Q., Wang, X., Liu, B., Yu, Z.-L., He, P.-B., Wan, Q., Cai, M.-Q., Yu, H.-L.: Geometric structure and photovoltaic properties of mixed halide germanium perovskites from theoretical view. Organic Electr. **53**, 50–56 (2018b). https://doi.org/10.1016/j.orgel.2017.11.005

Zhou, X., Jankowska, J., Dong, H., Prezhdo, O.V.: Recent theoretical progress in the development of perovskite photovoltaic materials. J. Energy Chem. **27**, 637–649 (2018). https://doi.org/10.1016/j.jechem.2017.10.010

Zhou, Y., You, L., Wang, S., Ku, Z., Fan, H., Schmidt, D., Rusydi, A., Chang, L., Wang, L., Ren, P., Chen, L., Yuan, G., Chen, L., Wang, J.: Giant photostriction in organic–inorganic lead halide perovskites. Nat. Commun. **7**, 11193 (2016). https://doi.org/10.1038/ncomms11193

Zhumekenov, A.A., Saidaminov, M.I., Haque, M.A., Alarousu, E., Sarmah, S.P., Murali, B., Dursun, I., Miao, X.-H., Abdelhady, A.L., Wu, T., Mohammed, O.F., Bakr, O.M.: Formamidinium lead halide perovskite crystals with unprecedented long carrier dynamics and diffusion length. ACS Energy Lett. **1**, 32–37 (2016). https://doi.org/10.1021/acsenergylett.6b00002

Authors and Affiliations

Sheikh Joifullah[1] · **Md. Adil Hossain**[1] · **Maruf Al Yeamin**[1] · **Md. Mahfuzul Haque**[1] · **Redi Kristian Pingak**[2] · **Noorhan F. AlShaikh Mohammad**[3] · **Mohammed S. Abu-Jafar**[4] · **Ahmad A. Mousa**[5,6] · **Asif Hosen**[1]

✉ Mohammed S. Abu-Jafar
mabujafar@najah.edu

✉ Asif Hosen
asif@mse.kuet.ac.bd

[1] Department of Materials Science and Engineering, Khulna University of Engineering and Technology (KUET), Khulna 9203, Bangladesh

[2] Department of Physics, Faculty of Science and Engineering, the University of Nusa Cendana, Kupang 85001, Indonesia

[3] Department of Physics, Faculty of Applied Sciences, Palestine Technical University, Tulkarm, Palestine

[4] Department of Physics, An-Najah National University, Nablus, Palestine

[5] Middle East University, Amman 11831, Jordan

[6] Applied Science Research Center, Applied Science Private University, Amman, Jordan